








Infrared Emission from Cold Gas Dusty Disks in Massive Ellipticals

Zhaoming Gan^{1,2} , Brandon S. Hensley^{3,5} , Jeremiah P. Ostriker¹ , Luca Ciotti⁴ , David Schiminovich¹, and Silvia Pellegrini⁴ 

¹ Department of Astronomy, Columbia University, 550 W. 120th Street, New York, NY 10027, USA

² New Mexico Consortium, Los Alamos, NM 87544, USA

³ Department of Astrophysical Sciences, Princeton University, Princeton, NJ 08544, USA

⁴ Department of Physics and Astronomy, University of Bologna, via Piero Gobetti 93/2, I-40129 Bologna, Italy

Received 2019 December 12; revised 2020 July 21; accepted 2020 August 4; published 2020 September 16

Abstract

What is the expected infrared output of elliptical galaxies? We report the latest findings obtained in this high time resolution (~ 10 yr) and high spatial resolution (2.5 pc at center) study. We add a set of grain physics to the Massive active galactic nucleus (AGN) Controlled Ellipticals Resolved code, including (a) dust grains made in passive stellar evolution; (b) dust grain growth due to collision and sticking; (c) grain destruction due to thermal sputtering; (d) dust cooling of hot gas via inelastic collisions; and (e) radiation pressure on dust grains. The code improvements enable us to analyze metal depletion and AGN obscuration due to dust, and to assess its infrared output. We simulate a representative massive elliptical galaxy of a central stellar velocity dispersion ~ 260 km s⁻¹ and modest rotation. We find that: (1) the circumnuclear disk (~ 1 kpc in diameter) is dusty in its outer region where most of the metals are contained in dust grains, while in the inner disk, dust grains are mostly destroyed by the AGN irradiation; (2) the dusty disk is optically thick to both the starlight within the disk and the radiation from the central AGN; thus the AGN is obscured behind the disk, and the covering factor is ~ 0.2 ; and (3) the duty cycles of the AGN activities, star formation, and the dust infrared luminosity roughly match observations; e.g., in most of its lifetime, the simulated galaxy is a stereotypical “quiescent” elliptical galaxy with $L_{\text{IR}} \sim 10^{11} L_{\odot}$, but it can reach $\gtrsim 10^{46}$ erg s⁻¹ during outbursts with a star formation rate $\gtrsim 250 M_{\odot}$ yr⁻¹.

Unified Astronomy Thesaurus concepts: [Black hole physics \(159\)](#); [Elliptical galaxies \(456\)](#); [E+A galaxies \(424\)](#); [Galaxy evolution \(594\)](#); [Interstellar medium \(847\)](#); [Interstellar dust \(836\)](#); [Metallicity \(1031\)](#); [Dust continuum emission \(412\)](#)

1. Introduction

The classic picture of massive elliptical galaxies imagines a quasi-spherical system filled with old, low-mass stars and hot, thermal X-ray emitting, moderately metal-rich gas. In fact evidence amassed over decades suggests that the central regions often contain significant amounts of cold gas, dust, and young stars. As early as the mid 1970s, Knapp and associates authored several papers on the central regions of normal elliptical galaxies with significant evidence for dust (e.g., Knapp 1975; Knapp et al. 1978). The prevalence of central dusty disks was noted as far back as van Dokkum & Franx (1995). Early guesses for the origin of the observed cold component include cooling flows and mergers. However, there has been very little work done to try to understand and model these phenomena, for two reasons. First, the standard cosmological codes have a spatial resolution of roughly in the range 0.1–1.0 kpc (Sijacki et al. 2015; Hopkins et al. 2018), so they are not equipped to study phenomena occurring in the inner 50 pc of these systems. Second, the prevailing characterization of these systems as “quiescent” make evidence for cold gas and star formation seem “anomalous.”

Our previous work at high resolution (inner radius ~ 2.5 pc) has shown us that intermittent cooling flows are a normal part of the evolution of these systems. Consequently, cool gas collects in central nuclear disks, inducing both feeding of the central black holes and episodes of star formation characterized by a top-heavy initial mass function (IMF). In this paper, we turn our focus to the resultant infrared (IR) output and compare

with observations. We will see that the cold gas component can exceed $10^{10} M_{\odot}$ at certain times with the dust mass exceeding $10^8 M_{\odot}$ in accordance with the Atacama Large Millimeter/submillimeter Array (ALMA)/SCUBA-2 observations such as those by Dudzevičiūtė et al. (2020) and Lang et al. (2019).

In this series of papers, our aim is to simulate and to understand the black hole feeding and active galactic nucleus (AGN) feedback processes in isolated massive elliptical galaxies. We also use the results from cosmological simulations to guide our implementation of cosmic accretion and its chemical properties. For example, Choi et al. (2017) performed zoom-in cosmological simulations on individual galaxies to study the effects of AGN feedback and the chemical evolution in the galaxies and their surroundings (see also Eisenreich et al. 2017; Brennan et al. 2018). In our Massive AGN Controlled Ellipticals Resolved (MACER) simulations, a relatively complete set of stellar physics has been incorporated, including asymptotic giant branch (AGB) stars, and type I and II supernovae (SNe I and II, respectively). We calculate the nucleosynthesis output from the stars and thereby track the chemical evolution in the modeled galaxies. Following Choi et al. (2017), we add a suite of chemical abundances to the code, solving 12 additional continuity equations for H, He, C, N, O, Ne, Mg, Si, S, Ca, Fe, and Ni, respectively, with metal yields from dying stars based on standard stellar physics (Gan et al. 2019a). With the high resolution of a few parsecs in central regions, we can track the metal enrichment, transportation, and dilution throughout the modeled galaxies. For example, we paid special attention to the chemical composition of the broad absorption line (BAL) winds. We find that the

⁵ Spitzer Fellow.

simulated metallicity in the BAL winds could be up to $\sim 8Z_{\odot}$, matching well with Sloan Digital Sky Survey observations of broad-line region gas (Nagao et al. 2006; Xu et al. 2018).

In our previous MACER simulations, we have not corrected for the depletion of metals onto dust, while the fractional depletion of refractory elements onto dust grains may be a large correction in the cold gas component, e.g., in/around the circumnuclear disk (see Hensley et al. 2014 for the case without rotation, nor metal tracers). Previous work on dust production in elliptical galaxies and its chemical effects can be also found in the papers by Calura et al. (2008); in the post-starburst phase, and Pipino et al. (2011) and Gall et al. (2011; during the starburst phase). In this paper, we will discuss our implementation of grain physics into the MACER code, and we will show how periodic outbursts of star formation and AGN activity can cause copious emission of IR radiation from the dust. The peak IR luminosity can reach 10^{46} erg s $^{-1}$. We organize the rest of the paper as follows: For completeness, we recall briefly the hydrodynamical equations and chemical tracers in Sections 2 and 3, respectively (see Gan et al. 2019a, 2019b for more details). In Section 4, we introduce the grain physics proposed by Hensley et al. (2014), and describe its implementation in the MACER code. In Section 5, we outline the additional physical processes that we have included. We focus on the observable infrared outputs in Section 6 and compare them with observations in Section 7. Finally, conclusions are presented in Section 8.

2. Hydrodynamics

We solve the time-dependent Eulerian equations that govern the hydrodynamics of the gaseous interstellar medium (ISM) over a length scale from 2.5 pc (inner boundary) to 250 kpc (outer boundary; Ciotti & Ostriker 1997; Novak et al. 2011; Gan et al. 2019b),

$$\frac{\partial \rho_{\text{gas}}}{\partial t} + \nabla \cdot (\rho_{\text{gas}} \mathbf{v}) = -\nabla \cdot \mathbf{T} - \dot{\rho}_{\star}^{+} + \dot{\rho}_{\text{II}} \cdot R_{\text{II,gas}} + \dot{\rho}_{\text{I}} \cdot R_{\text{I,gas}} + \dot{\rho}_{\star} \cdot R_{\star,\text{gas}} \quad (1)$$

$$\frac{\partial \mathbf{m}}{\partial t} + \nabla \cdot (\mathbf{m}\mathbf{v}) = -\nabla p_{\text{gas}} - \nabla p_{\text{rad}} - \rho_{\text{gas}} \nabla \phi - \dot{\mathbf{m}}_{\star}^{+} - \nabla \cdot \Pi_{\text{vis}} - \nabla \cdot \Pi_{\text{T}} + \dot{\mathbf{m}}_{\text{S}} + \rho_{\text{gas}} \cdot \mathbf{f}_{\text{rad,dust}}, \quad (2)$$

$$\frac{\partial E}{\partial t} + \nabla \cdot (E\mathbf{v}) = -p_{\text{gas}} \nabla \cdot \mathbf{v} + H - C + \dot{E}_{\text{T}} - \dot{E}_{\star}^{+} - \Pi_{\text{vis}} : \nabla \mathbf{v} + \dot{E}_{\text{II}} + \dot{E}_{\text{I}} + \dot{E}_{\text{S}} - H_{\text{dust,collision}}^{\text{gas}}, \quad (3)$$

where ρ_{gas} , \mathbf{m} , and E are the mass, momentum, and energy densities for the gaseous ISM, respectively. As usual, p_{gas} is the gas thermal pressure, and \mathbf{v} is its velocity. The adiabatic index is fixed to $\gamma = 5/3$. We refer the readers to our code paper (Gan et al. 2019b, and references therein) for the details of the physics we added in the simulation. We assemble the galaxy dynamics, stellar evolution, and atomic physics into our hydrodynamical simulations in the form of source/sink terms and boundary conditions, which are outlined briefly as follows:

1. *Galaxy dynamics* of rotating elliptical galaxies. Detailed modeling of the galaxy dynamics, including the gravitational potential ϕ and the stellar mass distribution (of total mass M_{\star}), are taken as the “background” of the simulation (see Section 5.1). Rotation is allowed and

determined self-consistently by solving the Jeans’ equations.

2. *Stellar evolution*. Passive stellar evolution is considered as mass and energy sources (Ciotti & Ostriker 2012; Pellegrini 2012), including AGB stars ($\dot{\rho}_{\star}$, \dot{E}_{S}), SNe Ia ($\dot{\rho}_{\text{I}}$, \dot{E}_{I} ; from the aged stellar population mentioned above), and SNe II ($\dot{\rho}_{\text{II}}$, \dot{E}_{II} ; if any, due to star formation; see below), where $R_{\star,\text{gas}}$, $R_{\text{I,gas}}$, and $R_{\text{II,gas}}$ (see Equation (11)) are the mass fractions of the stellar ejecta in the forms of gaseous chemical elements (see Equation (4)), while the rest are in the form of dust grains (see Equation (6)).
3. *Toomre instability* in the circumnuclear disk. We assume that the stellar mass loss inherits the velocity of its host stars (thus it contributes as a momentum source term $\dot{\mathbf{m}}_{\text{S}}$). Consequently, a circumnuclear disk will form from infalling gas because of the angular momentum barrier (e.g., Sarzi et al. 2006; Davis et al. 2011; Tadaki et al. 2018), and will inevitably become gravitationally unstable when gas accumulates continuously (i.e., the Toomre instability; Toomre 1964; Bertin & Lodato 1999; Goodman 2003; Jiang & Goodman 2011; Frazer & Heitsch 2019). Therefore, efficient mass accretion is possible by virtue of the Toomre instability, which will induce an inflowing mass flux \mathbf{T} (calculated from Equations (13)–(15) in Gan et al. 2019b), and it is also capable in transferring angular momentum (Π_{T}) outwards and dissipating energy (\dot{E}_{T}). Thus black hole accretion through the disk is possible.
4. *Star formation*. As another consequence of the gravitational instability, star formation is inevitable (see Section 5.2). Star formation is a sink for mass, momentum, and energy ($\dot{\rho}_{\star}^{+}$, $\dot{\mathbf{m}}_{\star}^{+}$, and \dot{E}_{\star}^{+} , respectively), consuming a significant fraction of the accreting mass before it can reach the central supermassive black hole. We assume a top-heavy IMF for the new stars, as evidenced by the central young stellar populations in the Milky Way (MW) and M31, and as argued by Bartko et al. (2010; see also Levin & Beloborodov 2003; Lu et al. 2013; Calzetti et al. 2015; Palla et al. 2020). Then, the distribution and age of the new stars sets the SNe II explosion rate.
5. *Alpha viscosity* is included to mimic the angular momentum transfer due to the magnetorotational instability (MRI). Besides the Toomre instability, the MRI can also transfer angular momentum (Π_{vis} ; Shakura & Sunyaev 1973; Balbus & Hawley 1998). Though it is inefficient on the length scale of interest, the MRI will still take effect on the timescale we simulate.
6. *AGN feedback* in the forms of both radiation and wind. We chose an inner boundary of 2.5 pc, which is within the fiducial Bondi radius, so that we can track the mass inflow onto the galaxy center self-consistently. We include a “sub-grid” AGN model (Ostriker et al. 2010; Yuan et al. 2018) to allow for both the radiation and wind output from the black hole accretion disk based primarily on observations of AGN outbursts (Arav et al. 2013, 2018; Kara 2018). Finally, we evaluate the AGN radiative feedback by calculating the metallicity-dependent radiative heating/cooling processes under the AGN irradiation ($H - C$; ∇p_{rad} is the radiation pressure; Sazonov et al. 2005), and evaluate the AGN mechanical feedback by injecting the wind output directly into the computational domain via the inner boundary. The adopted AGN wind speed in the cold mode is set to be

Table 1
Mass Fraction of the Elements from Various Sources

	AGBs ^a	SNe Ia ^b	SNe II ^c	CGM ^d	Solar ^e	Dust ^f
H	0.712859	0.000000	0.517998	0.746829	0.735972	0.000000
He	0.267027	0.000000	0.334833	0.251177	0.250628	0.000000
C	0.002939	0.002247	0.010310	0.000362	0.002411	0.171014
N	0.001834	0.000002	0.003618	0.000106	0.000706	0.000000
O	0.008723	0.074648	0.081750	0.000871	0.005849	0.293720
Ne	0.001895	0.002639	0.025177	0.000191	0.001271	0.000000
Mg	0.001064	0.011234	0.007615	0.000107	0.000713	0.117874
Si	0.000470	0.212119	0.003912	0.000101	0.000676	0.115942
S	0.001010	0.084995	0.008612	0.000047	0.000315	0.042512
Ca	0.000097	0.010865	0.000497	0.000010	0.000065	0.012560
Fe	0.001973	0.546927	0.005402	0.000198	0.001322	0.234783
Ni	0.000107	0.054323	0.000275	0.000001	0.000072	0.011594
Z ^g	0.020114	1.000000	0.147168	0.001994	0.013400	1.000000

Notes.

^a Averaged metal abundance of AGB winds over the time span from $t_{\text{age}} = 2$ to 13.7 Gyr, i.e., $\langle \dot{X}_{*,i} / \dot{\rho}_* \rangle$ (Karakas 2010).

^b Metal abundance of SNe Ia ejecta, i.e., $\dot{X}_{\text{I},i} / \dot{\rho}_{\text{I}}$ (Seitenzahl et al. 2013).

^c Metal abundance of SNe II ejecta, i.e., $\dot{X}_{\text{II},i} / \dot{\rho}_{\text{II}}$ (Nomoto et al. 2013).

^d Metal abundance of the low-metallicity infalling CGM, of which one-fourth is made of primordial gas and three-fourths low-metallicity gas of 0.2 solar abundance.

^e Solar abundance (Asplund et al. 2009).

^f Metal composition of dust grains, i.e., $\langle \bar{D}_i / \bar{\rho}_{\text{dust}} \rangle$.

^g Metallicity Z, i.e., mass fraction of all chemical species except H and He.

$6 \times 10^3 \text{ km s}^{-1}$ (Arav et al. 2018) with an efficiency of $\epsilon_w = 1.5 \times 10^{-3}$. The initial black hole mass is taken to be $10^{-3} M_*$ (see Table 2).

7. *Cosmic accretion* through the galaxy outskirts. We allow circumgalactic medium (CGM) infall (cosmic accretion) at the outer boundary by injecting time-dependent inflows based on cosmological simulations (Choi et al. 2017; Brennan et al. 2018; see Gan et al. 2019b for more details). The CGM infall and AGN wind feedback are implemented as boundary conditions; thus they will not appear in the equations above. The total CGM infall mass is now set to be $16\% M_*$, and the infall velocity is set at 50% of the freefall velocity.

8. *Radiation pressure on dust grains.* Due to the high dust opacity, the radiation pressure on the dust grains ($f_{\text{rad,dust}}$; see Equation (22)) can be much higher than that on the electrons. In our simulations, we assume the dust grains are coupled with gas dynamics, and so the radiation pressure on the dust will be an important mechanism regulating the gas flow, especially during the outbursts of the AGN.

9. *Dust cooling of hot gas.* In the densest zone in the circumnuclear disk (where the gas density reaches $> 10^5 \text{ atom cm}^{-3}$), most of the metals are in dust grains. There, the frequent collisions between gas and dust particles ($H_{\text{dust,collision}}^{\text{gas}}$; see Equation (18)) will cool down the gas efficiently on a timescale as short as ~ 1 yr. Therefore, dust cooling is an important mechanism in the simulation to allow the gas to be further cooled down below 10^4 K.

The ISM hydrodynamical equations, together with the tracers for metals and dust, are solved by using the grid-based Athena++ code (version 1.0.0; Stone et al. 2008) in spherical coordinates. We assume axisymmetry but allow rotation. The outer boundary is chosen as 250 kpc to enclose the whole massive elliptical galaxy, and the inner boundary R_{in} is set to be

2.5 pc to resolve the Bondi radius. We use a logarithmic grid ($\Delta r_{i+1} / \Delta r_i = 1.1$) to divide the radial axis into 120 discrete cells. The azimuthal angle θ is divided into 30 uniform cells and covers an azimuthal range from 0.05π to 0.95π . The numerical solver for the gas dynamics is composed of the combination of the HLLC Riemann Solver, the PLM reconstruction, and the second-order van Leer integrator. We start the simulations when the initial stellar population is 2 Gyr old, i.e., after the major phase of galaxy formation; we therefore maintain the galaxy structure and internal kinematics fixed during the simulations.

3. Chemical Abundances

In Gan et al. (2019a), we tracked the chemical evolution of H, He, and metals by using 12 tracers X_i ($i = 1, 2, \dots, 12$; mass of each element per unit volume) for H, He, C, N, O, Ne, Mg, Si, S, Ca, Fe, and Ni, respectively (inspired by Choi et al. 2017; Eisenreich et al. 2017 for large-scale simulations using smoothed particle hydrodynamics). We solve 12 additional continuity equations of the tracers, assuming the chemical species co-move once after they are injected into the ISM, i.e.,

$$\frac{\partial X_i}{\partial t} + \nabla \cdot (X_i \mathbf{v}) + \nabla \cdot \mathbf{T}_i = \dot{X}_{*,i} + \dot{X}_{\text{I},i} + \dot{X}_{\text{II},i} - \dot{X}_{*,i}^+, \quad (4)$$

where

$$\mathbf{T}_i = (X_i / \rho_{\text{gas}}) \cdot \mathbf{T}, \quad \dot{X}_{*,i}^+ = (X_i / \rho_{\text{gas}}) \cdot \dot{\rho}_*^+, \quad (5)$$

and \mathbf{v} is obtained by solving the hydrodynamical equations as usual. Here \mathbf{T}_i is the inflowing mass flux of chemical species i induced by the Toomre instability. The products of stellar evolution in Equation (4), i.e., AGB stars ($\dot{X}_{*,i}$), SNe Ia ($\dot{X}_{\text{I},i}$), and SNe II ($\dot{X}_{\text{II},i}$), serve as sources of metals with each having different compositions (see Table 1). The time-dependent metal yields above are calculated assuming standard stellar physics

(Saitoh 2017; Gan et al. 2019a). The advection terms $\nabla \cdot (X_i \mathbf{v})$ and $\nabla \cdot \mathbf{T}_i$ describe the transport and the mixing of ISM with different metal abundances. Star formation ($\dot{X}_{*,i}^+$) is treated as a sink of metals, but does not to change the local relative abundances.

On the galaxy outskirts, we include the cosmic accretion (i.e., CGM infall). The CGM has low metallicity by construction (see Table 1); therefore it will dilute the metallicity as it falls into the galaxy and mixes with the ISM there. At the inner boundary of the simulation domain, we also recycle the metals via the BAL winds, which are injected back to the galaxy by the central AGN. The metal abundance of the inflow at our innermost grid point (Ciotti & Ostriker 1997; Gan et al. 2019b). Finally, we assume the abundance of the initial ISM (see Section 5.1) is $Z \sim 1.54Z_\odot$ (where Z_\odot is the solar metallicity; Asplund et al. 2009). The initial abundance of $1.54Z_\odot$ is adopted from the zoom-in cosmological simulations by Choi et al. (2017) for elliptical galaxies of similar mass as in our galaxy model (see also Eisenreich et al. 2017).

It is a goal of this paper to evaluate the depletion of metals onto dust, especially in the cold gas component; the fractional depletion of refractory elements onto dust grains may be a large correction. The total infrared radiation from the dust may be comparable to or greater than the X-rays from the hot gas.

4. Grain Physics

4.1. Grain Hydrodynamics

Dust grains are injected into the ISM by both AGB winds and supernovae. Grains are quickly coupled to gas via collisions, and so they are passively advected. Collisions with hot gas atoms can erode grains, while dust in cold gas can grow via accretion of metals. In parallel to the treatment of metals (Equation (4)), we implement these processes in a dust continuity equation (see also Hensley et al. 2014):

$$\frac{\partial \rho_{\text{dust}}}{\partial t} + \nabla \cdot (\rho_{\text{dust}} \mathbf{v}) + \nabla \cdot \mathbf{T}_{\text{dust}} = \dot{\rho}_{*,\text{dust}} - \dot{\rho}_{*,\text{dust}}^+ + \dot{\rho}_{\text{dust,gg}} - \dot{\rho}_{\text{dust,gd}}, \quad (6)$$

where

$$\mathbf{T}_{\text{dust}} = (\rho_{\text{dust}} / \rho_{\text{gas}}) \cdot \mathbf{T}, \quad \dot{\rho}_{*,\text{dust}}^+ = (\rho_{\text{dust}} / \rho_{\text{gas}}) \cdot \dot{\rho}_*^+, \quad (7)$$

are the mass advection and sink terms due to the Toomre instability and star formation, respectively.

The mass density X_i of each element i is given by Equation (4). We partition this into a gas-phase density G_i and a density in dust grains D_i , i.e.,

$$X_i = G_i + D_i. \quad (8)$$

X_i and ρ_{dust} can be solved from the continuity Equations (4) and 6, respectively. To derive G_i and D_i , we assume for simplicity that all grains have a fixed composition. Table 1 lists the assumed mass fraction of each metal in dust $\langle \tilde{D}_i / \tilde{\rho}_{\text{dust}} \rangle$. Thus, D_i is given by

$$D_i \equiv \rho_{\text{dust}} \cdot \langle \tilde{D}_i / \tilde{\rho}_{\text{dust}} \rangle, \quad (9)$$

with G_i following from Equation (8). This formulation allows us to track the time evolution and the spatial distribution of each chemical species in the gaseous ISM and in dust.

The source term $\dot{\rho}_{*,\text{dust}}$ in Equation (6) describes the injection of dust grains into the ISM from dying stars, including both AGB winds and supernovae. Specifically,

$$\dot{\rho}_{*,\text{dust}} = \dot{\rho}_* \cdot R_{*,\text{dust}} + \dot{\rho}_I \cdot R_{I,\text{dust}} + \dot{\rho}_{II} \cdot R_{II,\text{dust}}, \quad (10)$$

where $R_{*,\text{dust}}$, $R_{I,\text{dust}}$, and $R_{II,\text{dust}}$ are the maximum ratios of dust mass to the total ejecta of AGB stars, SN Ia, and SN II, respectively, when the total available metals are transformed to the dust phase, e.g.,

$$R_{*,\text{dust}} = 1 - R_{*,\text{gas}} = \min_{i=1 \dots 12} \left(\frac{\dot{X}_{*,i} / \dot{\rho}_*}{D_i / \rho_{\text{dust}}} \right). \quad (11)$$

That is, we assume that each of these sources injects as much dust of our prescribed composition—numerically, we “make” dust grains from the stellar metal yields until any of the metal ingredients runs out, then no more dust grains can be made according to the fixed dust chemical composition, i.e., each planetary nebula makes as much dust as its ejected metals permit. We calculate $(R_{I,\text{dust}}, R_{I,\text{gas}})$ and $(R_{II,\text{dust}}, R_{II,\text{gas}})$ in a similar way.

Finally, we track the mass exchange between the gaseous ISM and the dust by allowing grain growth $\dot{\rho}_{\text{dust,gg}}$ and grain destruction $\dot{\rho}_{\text{dust,gd}}$. These are described in more detail in the following sections.

4.2. Grain Destruction

In hot gas, impacting ions can erode dust grains on short timescales (Draine & Salpeter 1979). Thermal sputtering is expected to be the dominant grain destruction process in the hot ISM of an elliptical galaxy. Following Hensley et al. (2014), we adopt an analytic approximation for the sputtering rate that depends only on the gas density and temperature (Draine 2011). Letting a be the grain radius, T_6 the gas temperature in units of 10^6 K, and n_{H} the proton number density in units of cm^{-3} ,

$$\dot{a} = - \frac{10^{-6} n_{\text{H}}}{1 + T_6^{-3}} \mu\text{m yr}^{-1}. \quad (12)$$

We assume that the grain size distribution is everywhere given by the Mathis–Rumpl–Nordsieck (Mathis et al. 1977) size distribution, i.e.,

$$\frac{dn_d}{da} = \frac{Aa^{2.5}}{a^{3.5}} \quad (13)$$

where $(dn_d/da)da$ is the number density of grains with sizes between a and $a+da$. A is a normalization factor that can be determined from the total dust mass density ρ_{dust} via

$$\rho_{\text{dust}} = \frac{8\pi}{3} A (1 - \sqrt{a_{\text{min}}/a_{\text{max}}}) \rho_{\text{grain}} a_{\text{max}}^3, \quad (14)$$

where ρ_{grain} is the mass density of a dust grain, taken to be 3.5 g cm^{-3} as typical for a silicate grains (Draine & Lee 1984). Guided by Mathis et al. (1977) and Weingartner & Draine (2001), we adopt $a_{\text{min}} = 0.005 \mu\text{m}$ and $a_{\text{max}} = 0.3 \mu\text{m}$. The total destruction rate is obtained by integrating the mass destruction rate

of grains of radius a over the size distribution, i.e.,

$$\dot{\rho}_{\text{dust,gd}} = 8\pi A \rho_{\text{grain}} \left(\frac{a_{\text{max}}}{a_{\text{min}}} \right)^{0.5} a_{\text{max}}^2 \dot{a}. \quad (15)$$

This implementation of thermal sputtering implicitly assumes that the all of the gas in a cell can be described by a single temperature. However, cool, dense gas can be shock heated by supernovae, creating conditions favorable for nonthermal sputtering and grain–grain collisions at spatial scales not resolved by the simulation (Seab & Shull 1983). Grain destruction by supernova-driven shocks has been implemented in other studies by coupling the grain destruction timescale to the supernova rate (e.g., McKinnon et al. 2016; Zhukovska et al. 2016). Given the nature of the hot ISM of an elliptical galaxy and the necessarily phenomenological approach needed to incorporate this sub-grid physics, we do not consider this destruction mechanism in this work. However, as we discuss in Section 7.2, this may lead to an overestimate of the dust content in cool gas in the simulation.

4.3. Grain Growth

When the gas density is sufficiently high, dust grains can grow from the accretion of metal atoms from the gas phase (Hensley et al. 2014, and references therein). Assuming a sticking efficiency f and average speed v_Z of these metal atoms, the grain growth rate due to collisions is $f\rho_Z v_Z 4\pi a^2 n_d$, where ρ_Z is the mass density of the metals available for grain growth, i.e.,

$$\rho_Z = \rho_{\text{gas}} \cdot \min_{i=1 \dots 12} \left(\frac{G_i / \rho_{\text{gas}}}{D_i / \rho_{\text{dust}}} \right). \quad (16)$$

In this formulation, $\rho_Z \rightarrow 0$ when any of the atomic constituents of dust (see Table 1) has been significantly depleted from the gas phase, thereby limiting the efficiency of grain growth.

Integrating over the grain size distribution, we obtain

$$\dot{\rho}_{\text{dust,gg}} = f\rho_Z \frac{c_s}{\sqrt{\mu_Z}} 8\pi A a_{\text{max}}^2 \left(\frac{a_{\text{max}}}{a_{\text{min}}} \right)^{0.5}. \quad (17)$$

In the equation above, we have made the approximation $v_Z = c_s / \sqrt{\mu_Z}$, where c_s is the sound speed of the gas, and μ_Z is the mean atomic mass of the metal atoms. For simplicity, we set constant $f = 0.2$ and $\mu_Z = 16$.

4.4. Dust Cooling of Hot Gas

It is known that dense ISM will be cooled down efficiently via inelastic collisions with dust grains (Ostriker & Silk 1973; Smith et al. 1996; Draine 2011). The cooling rate of gas per unit volume per unit time can be written as,

$$H_{\text{dust,collision}}^{\text{gas}} = \int_{a_{\text{min}}}^{a_{\text{max}}} da \frac{dn_d}{da} \cdot 4\pi a^2 \cdot \frac{1}{2} \rho_{\text{gas}} c_s^3 \cdot \left[1 + \frac{T_4}{1 + T_4} \left(\frac{m_p}{m_e} \right)^{\frac{1}{4}} \right], \quad (18)$$

where T_4 is the gas temperature in units of 10^4 K. The factor in the brackets is a correction for the energy exchange considering the charge of dust grains and that electrons dominate the collisions when the gas temperature is high.

In the circumnuclear disk, both the gas density and dust density can be very high, which makes the process above very efficient—its timescale could be as short as $\lesssim 1$ yr. Therefore, it is a stiff sink term in the energy equation of the gas dynamics, and it is numerically expensive to resolve the timescale explicitly. To overcome this difficulty, we assume thermal equilibrium when the timescale is shorter than the time step given by the Courant–Friedrichs–Lewy condition—we calculate the equilibrium temperature while assuming the thermal pressure is fixed. After that, we evaluate the energy loss according to the difference between the instantaneous gas temperature and the equilibrium temperature.

4.5. Radiation Pressure on Dust Grains

It is known that absorption by dust grains is the dominant sources of AGN obscuration, often exceeding the opacity due to electron scattering by orders of magnitude. The dust opacity in the UV, optical, and IR bands can be written roughly as,

$$\begin{aligned} \kappa_{\text{dust,opt}} &= 300 \times \left(\frac{\rho_{\text{dust}}}{\rho_{\text{gas}}} \right) \left(\frac{\rho_{\text{dust}}}{\rho_{\text{gas}}} \right)_{\text{MW}}^{-1} \text{ cm}^2 \text{ g}^{-1}, \\ \kappa_{\text{dust,UV}} &= 4\kappa_{\text{dust,opt}}, \quad \kappa_{\text{dust,IR}} = \kappa_{\text{dust,opt}}/150 \end{aligned} \quad (19)$$

where we have scaled the opacities according to the dust-to-gas ratio normalized by the MW value. For simplicity, we only consider the absorption of UV photons from the central AGN by dust grains. The photon energy absorbed by dust grains per unit volume per unit time can be written as

$$H_{\text{dust,abs}}^{\text{AGN,UV}} = \rho_{\text{dust}} \kappa_{\text{dust,UV}} \cdot \frac{L_{\text{AGN,UV}}}{4\pi r^2} \exp(-\tau_{\text{dust,UV}}) \quad (20)$$

where $L_{\text{AGN,UV}}$ is the AGN luminosity in the UV band. $\tau_{\text{dust,UV}}$ is the optical depth of dust in the UV band along radial directions, i.e.,

$$\tau_{\text{dust,UV}} = \int_{r_{\text{in}}}^r \rho_{\text{dust}} \kappa_{\text{dust,UV}} \cdot dr'. \quad (21)$$

The calculation of the optical depth above is very computationally expensive because it could not be parallelized. For the sake of computational efficiency, we update the optical depth only every 100 time steps.

The dust grains gain momentum when they absorb the photons, which results in the radiation pressure on dust grains. Compared to electron scattering, the radiation pressure due to irradiation by AGNs could be very significant especially during bursts. Since we assume that the dust grains are coupled with gas dynamics, there will be a net acceleration to the gas as follows (Draine 2011):

$$\mathbf{f}_{\text{rad,dust}} = \frac{\rho_{\text{dust}} \kappa_{\text{dust,UV}}}{\rho_{\text{gas}} + \rho_{\text{dust}}} \cdot \frac{L_{\text{AGN,UV}}}{4\pi r^2 c} \exp(-\tau_{\text{dust,UV}}) \cdot \hat{\mathbf{r}}. \quad (22)$$

4.6. Initial and Boundary Conditions for Dust

At the inner boundary, we keep track of the dust accreted onto the black hole accretion disk. Since the temperature of the black hole accretion disk (even in the cold mode) is high enough so that no dust can survive, we return the metals in dust grains (which are accreted onto the center) back to the gas phase where they are ejected in the BAL winds. For simplicity,

Table 2
Parameters of the Initial Galaxy Model

Galaxy Property	Value	Description
L_B	$1.25 \times 10^{11} L_{B\odot}$	total stellar luminosity
M_*	$6.1 \times 10^{11} M_\odot$	total stellar mass
R_e	11.36 kpc	projected half-light radius
M_g	$1.22 \times 10^{13} M_\odot$	total mass of the galaxy
σ_*	260 km s ⁻¹	1D velocity dispersion at $0.1R_e$
ϵ	0.37	ellipticity
M_{BH}	$6.1 \times 10^8 M_\odot$	initial mass of central black hole

we assume the BAL wind is dust free, as it can be easily heated up by shocks, which will make it difficult for dust to survive.

At the outer boundary, we allow for inflows of low-metallicity material ($Z = 0.15Z_\odot$; see Table 1) to mimic the CGM infall. For simplicity, we assume that the CGM is dust free.

Finally, we assume that the initial ISM is dust free as its temperature is high.

5. Adjustments to the Numerical Models

5.1. Initial Galaxy Model

The simulation in this paper is designed for an isolated, massive elliptical galaxy, such as NGC 5129. The galaxy model is built using the procedure described in Gan et al. (2019b), and its main properties are summarized in Table 2 (see also Bentz & Manne-Nicholas 2018; S. Pellegrini et al. 2021, in preparation). The only difference is a radius-dependent description of the Satoh’s k -parameter that is now parameterized as

$$k(r) = k_0 + (k_{\text{est}} - k_0) \cdot \frac{r}{r_0 + r}, \quad (23)$$

where $k_0 = 0.42$, $k_{\text{est}} = 0.05$, $r_0 = 40$ kpc. These parameters produce a rather flat rotation curve, which approximates $v_{\text{rot}} \sim 100$ km s⁻¹ when $r \lesssim R_e$, and then decreases outward in order to reproduce qualitatively the main features of the rotation profile of NGC 5129.

In our standard simulations, we start with a gas-free galaxy allowing infall and stellar evolution to provide all of the subsequent ISM. In our results section (Section 6.4), we will also describe the results of a perhaps more plausible initial state where the gas/star mass ratio at the beginning of the simulation is $\sim 30\%$.

5.2. Star Formation Criterion

In our model, we have two physical channels for star formation, i.e., one via the Toomre instability, when the disk is gravitationally unstable (Toomre 1964; Goodman 2003; Jiang & Goodman 2011), and the other via radiative cooling when it is Jeans unstable. To ensure it is gravitationally unstable at the site of star formation, we allow star formation due to radiative cooling only when the local Jeans radius is smaller than the cell height. The Jeans radius reads,

$$R_{\text{Jeans}} = 3 \times \left(\frac{c_s}{2 \text{ km s}^{-1}} \right) \sqrt{\frac{10^3 \text{ cm}^{-3}}{n_H}} \text{ parsec}. \quad (24)$$

We have not made an allowance for shear or turbulence velocities within cells; these effects would reduce star formation in the innermost regions.

5.3. Cooling Radius of Supernovae

In the densest zone on the circumnuclear disk, the cooling radius of SN II feedback can be very small, i.e., the SN II heating will fade before it can affect its distant surroundings. Therefore, we allow SN II heating only when its cooling radius is larger than the cell height. The cooling radius of an SN II is approximately

$$R_{\text{cool}} = 5 \times E_{51}^{1/5} n_H^{1/5} \left(\frac{t_{\text{cool}}}{10^3 \text{ yr}} \right)^{2/5} \text{ parsec}, \quad (25)$$

where E_{51} is the total energy output of an SN II explosion in units of 10^{51} erg, $t_{\text{cool}} = \min(t_{\text{low}}, t_{\text{high}})$ is the time of expansion of a supernova remnant before cooling. t_{low} and t_{high} are the estimates from the low- and high-temperature branches, respectively (see Kim & Ostriker 2015),

$$\begin{aligned} t_{\text{low}} &= 4 \times 10^4 E_{51}^{0.22} n_H^{-0.55} \text{ yr}, \\ t_{\text{high}} &= 4 \times 10^5 E_{51}^{0.38} n_H^{-0.55} \text{ yr}. \end{aligned} \quad (26)$$

5.4. Runaway Stars

In our previous model (e.g., Gan et al. 2019a), we assumed a top-heavy IMF for the star formation in the circumnuclear disk (Goodman & Tan 2004; Bartko et al. 2010; Lu et al. 2013; Palla et al. 2020), i.e., $\sim 60\%$ of the mass in new stars is in massive stars, of which a large fraction is in binary systems. Thus, there is a significant probability for the massive stars to be kicked out of the circumnuclear disk, typically, with a runaway speed greater than 30 km s⁻¹. Finally, the runaway stars explode outside the circumnuclear disk and heat the ISM there. Therefore, the runaway stars may be an additional heating source for the ISM in the central galactic regions, which is a direct consequence of the star formation in the circumnuclear disk. Thus, following Eldridge et al. (2011; their Figure 2), we assume that 40% of the massive stars are runaway stars, and sample the escaping speed of the runaway stars according to the fitting formula below for the observed cumulative distribution function (CDF),

$$v_{\text{runaway}} = 30 - 100 \log(1 - \text{CDF}) \text{ km s}^{-1}, \quad (27)$$

i.e., no runaway stars have $v_{\text{runaway}} < 30$ km s⁻¹, 50% of the stars have that $v_{\text{runaway}} < 60$ km s⁻¹, 90% of the stars have $v_{\text{runaway}} < 130$ km s⁻¹, etc. We set a fixed travel time for the runaway stars of 5×10^6 yr, while the direction of the runaway stars is sampled randomly with equal probability over the solid angle of 4π .

5.5. Mass-dependent Explosion Energy of SNe II

Previously, we assumed that all SNe II inject a single characteristic explosion energy of 10^{51} erg s⁻¹. However, the explosion energy of an SN II should be dependent on the mass of its progenitor. In this paper, we adopt the mass-dependent SN II explosion energy in Morozova et al. (2018; their Figure 6), fitting

it with the formula below,

$$\log(E_{\text{SNII}}) = 50.6 + 2.2 \log(M/10M_{\odot}) \quad \text{erg s}^{-1}. \quad (28)$$

5.6. Kinetic Feedback of SNe II

We now allow SN II kinetic feedback, i.e., we keep the vertical momentum component of the SN II ejecta, which corresponds to 1/16 of the total SN II energy, while the other 15/16 of the energy is still in form of thermal energy.

6. Results

As in our previous simulations, we found that a circumnuclear disk formed in the galaxy center, of which the size (half-mass–radius) is ~ 1 kpc, consistent with observations (Sarzi et al. 2006; Davis et al. 2011; Boizelle et al. 2017). The cold gas in the circumnuclear disk is replenished by a normal cooling flow modified by rotation. Most of time, the circumnuclear disk is quiet, but once it becomes sufficiently over-dense and self-gravitating, massive star formation occurs due to the gravitational instability (Burkhart & Mocz 2019). The latter also permits angular momentum transfer, and thus triggers mass accretion onto the central black hole, and therefore induces AGN outbursts after a time lag. Subsequently, the ample energy outputs from the AGN and SNe regulate the mass supply onto the circumnuclear disk, stabilize it from the gravitational instability, and force the whole galaxy into a quiescent state until another cycle begins (e.g., Ciotti & Ostriker 1997; Reynolds et al. 2015; Yang & Reynolds 2016).

The patterns of the galaxy activities are shown in Figure 1, in which we plot the history of mass supply to the galaxy center, AGN activities, and star formation. Very high time resolution (~ 10 yr in our simulation) is needed to compute and to visualize the activity, since most of the star formation and AGN output occur in episodes of very short duration. Note that while in early starbursts, star formation rates can exceed $250M_{\odot} \text{ yr}^{-1}$ and in later ones $\geq 20M_{\odot} \text{ yr}^{-1}$, in the quiescent intervals that dominate at late times (the last 1 Gyr in the simulation), the average star formation rate is less than $1.5M_{\odot} \text{ yr}^{-1}$ (as observed by, e.g., Kuntschner et al. 2010; Sarzi et al. 2013; Davis et al. 2014; see also Negri et al. 2015).

In general the galaxy is a prototypical “quiescent” elliptical galaxy, but star formation can exceed that in normal spirals during central outbursts. Thus, the top panels of Figure 1 may present a somewhat misleading visual estimate of the fraction of time during which there are starbursts or AGN activity; therefore in the lower panels, we show the same quantities averaged over a 10^8 yr timescale. In Figure 2, we present the duty cycle (i.e., fraction of time) spent at different levels of AGN activity and star formation. The left panel of Figure 2 shows that for only $\sim 0.5\%$ of its lifetime is the AGN in the quasar mode (i.e., if the AGN luminosity is larger than 10% of the Eddington limit, $L_{\text{BH}} > 0.1L_{\text{Edd}}$), while during such a short duty cycle, the AGN emits $\sim 8\%$ of its total energy output in the form of radiation.

We can see from the middle panel of Figure 1 that the instantaneous star formation rate is up to $> 100M_{\odot} \text{ yr}^{-1}$, while its duty cycle is extremely short ($\lesssim 1 \times 10^{-4}$; see the blue line in the right panel of Figure 2). The star formation rate is $< 2M_{\odot} \text{ yr}^{-1}$ during 59% of the galaxy’s lifetime.

In the remainder of this section, we focus on the dust, including its hydrodynamical and thermodynamical properties, and its infrared emission. In Section 6.1, we present the spatial

distribution of the dust and its effects of metal depletion and obscuration. In Section 6.2, we derive the thermal properties of the dust based on the outputs of our simulation. In Section 6.3, we present the infrared emission from dust and compare it with observations. Finally, we discuss the dependence of our results on the initial conditions and spatial resolution in Section 6.4.

6.1. Cold Gas Dusty Disk

In Figure 3, we show the hydrodynamical properties of the circumnuclear disk, including its gas and dust components, at the end of the simulation. We can see that the gas component of the circumnuclear disk is dense and cold, which is ideal for star formation and dust grain growth. In the upper-mid panel, we see that in most of the volume, the gas is virialized, with a typical temperature around 1 keV. In the circumnuclear disk, the gas can be cooled far below 10^4 K until it hits the temperature floor of 50 K, as we now allow for dust cooling of the hot gas. In the lower-left panel, we plot the dust density. In the lower-mid panel, we present the dust-to-gas mass ratio, which is up to ~ 0.1 . It is also much higher than the typical value in the solar neighborhood, which indicates that the dust depletion of metals can be very significant, though in the innermost part of the disk, AGN outbursts have efficiently destroyed all dust (Kawakatu et al. 2020).

To demonstrate the effects of dust depletion of metals, in Figure 3, we plot the gas metallicity and total (gas and dust) metallicity in the upper-right and lower-right panels, respectively. We can see that the metallicities are significantly enhanced in the inner region, but there is a void in the spatial distribution of the gas metallicity in the outer disk, which is coincident with the peak of the dust-to-gas mass ratio (see the lower-mid panel in Figure 3). In the bulk of the hot X-ray emitting gas, the metallicity is below the solar value on average in the late times, but the BAL winds can have a highly super-solar metal abundance. The innermost and outermost regions are nearly dust free, the former because of AGN activity, the latter due to the low metallicity of cosmological inflow gas. We note that the circumnuclear disk is dusty, especially in its outer region where most of the metals are in dust grains. In Figure 4, we present the mass distribution of Fe in the forms of gas and dust grains. We can see that the mass density of the gas-phase Fe peaks in the inner region of the circumnuclear disk, and it is spread into the polar regions due to the AGN winds. From the right panel of Figure 4, we can see the significant dust depletion of Fe; almost all of the Fe is in dust grains in the outer disk.

In Figure 5, we plot the surface density of the gas and dust components with blue and orange lines, respectively. The solid lines represent the results during an outburst at $t = 3.87$ Gyr, while the dashed lines show the results (at $t = 13.64$ Gyr) when the system is relatively quiescent. We can see from the figures above that the spatial distribution of dust overlaps with that of the gas component. But unlike the gas component, the dust density peaks in the outer disk rather than in the inner disk, as the gas temperature is relatively high in the inner disk due to the AGN feedback and supernova heating, which makes it difficult for the dust grains to survive.

In Figure 6, we plot the total mass of dust grains and gaseous ISM in different ranges of temperature. It shows that the total dust mass is typically $5 \times 10^7 M_{\odot}$, and the typical masses of the cold circumnuclear disk and the X-ray emitting hot ISM are $\sim 10^9$ and $10^{11} M_{\odot}$, respectively.

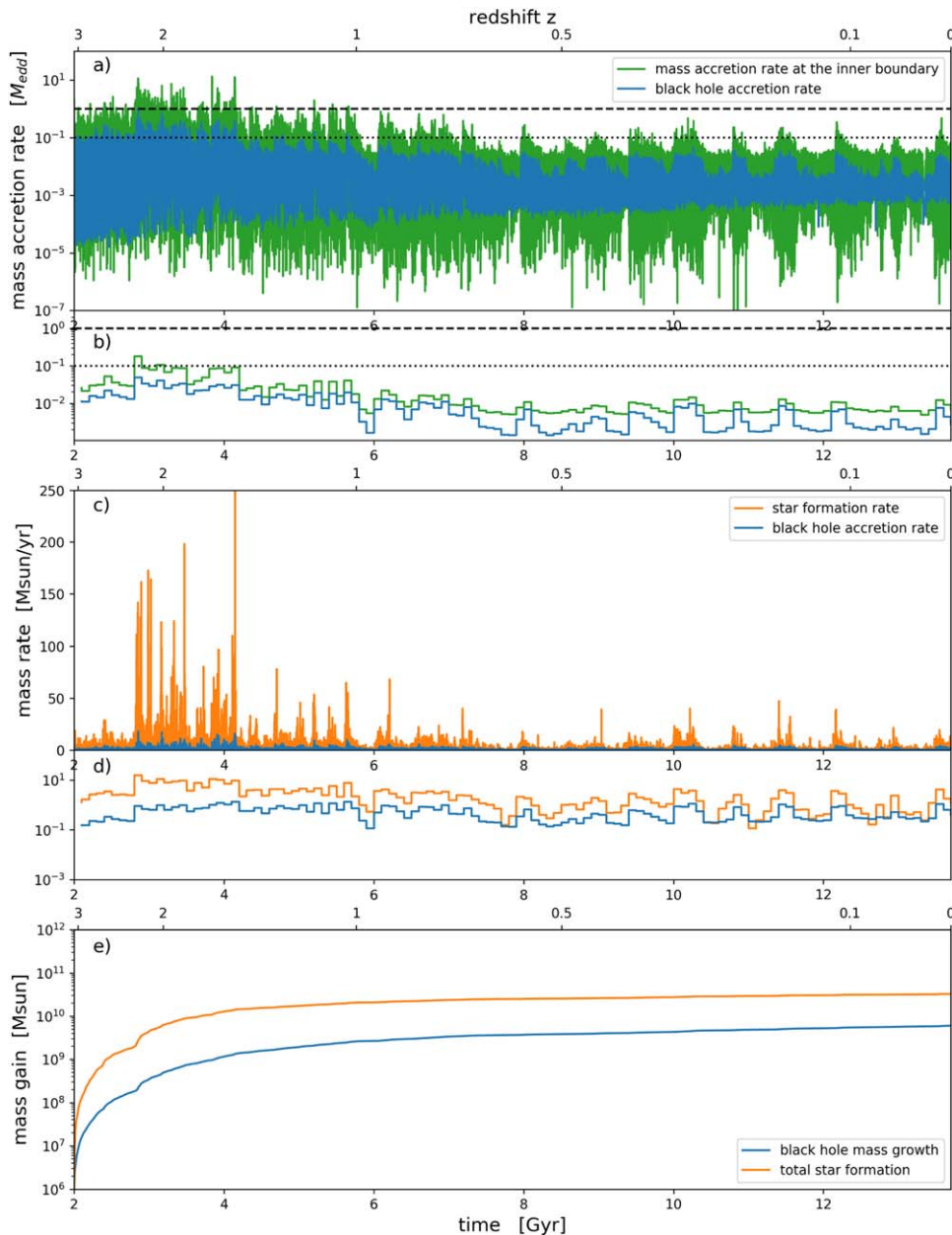


Figure 1. History of the mass supply onto the galaxy center, AGN activities, and star formation in the simulation. The time resolution in panels (a), (c), and (e) is ~ 10 yr, while panels (b) and (d) average over a 10^8 yr timescale.

Dust obscuration of photons is known to be very important in many astrophysical systems, especially at UV and optical wavelengths, and the dust opacity in AGN environments can dominate over electron scattering. In next subsection, we calculate the infrared emission from the dust, where the irradiation by the AGN and starlight is an important energy source for the dust emission. Therefore, it is useful to discuss below the dust obscuration of both the AGN radiation and the starlight in/through the circumnuclear disk.

Before we evaluate the dust absorption of starlight, we present in Figure 7 the cumulative star formation during the simulation. We can see that almost all of the star formation ($\sim 3.3 \times 10^{10} M_{\odot}$) is embedded in the dusty disk, where the gas is over-dense. The characteristic radius of the star-forming region is only ~ 20 pc and would be difficult to detect except in the nearest elliptical systems. Note that: (i) in our star formation

criterion (Section 5.2), we have not yet included the shear and turbulent velocity dispersion within cells. Allowing for this would reduce star formation in the innermost regions; and (ii) we do not include the dynamical and structural effects of the new stars, which may dominate the stellar mass and shift the dynamics significantly in the innermost region. One can expect that the new stars are an important source of UV photons that can be easily absorbed by dust grains, and thus can be effective in heating up the dust, and enabling the latter to emit in infrared.

In Figure 8, we plot the dust optical depth for the UV photons emitted in the circumnuclear disk during the starburst at $t_{\text{age}} = 4.13$ Gyr. For simplicity, the optical depth is integrated along the θ -direction. Again, we can see that the dusty disk is optically thick to the starlight, i.e., most of the stellar radiation is expected to be absorbed within the disk, and

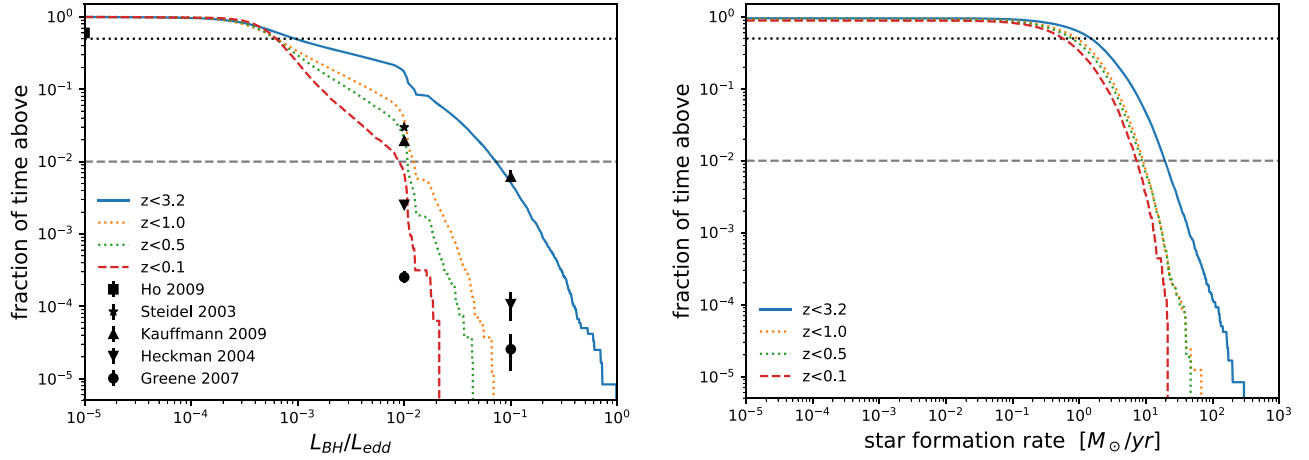


Figure 2. Duty cycle of the AGN activities (left panel) and star formation (right panel), i.e., the fraction of time when the quantities are the above given values. The horizontal dotted lines are at 50% and dashed lines are at 1%. The colored lines are the simulation results below the given redshift. The points in the left panel are observational constraints. The star is a constraint compiled from high-redshift observations by Steidel et al. (2003). The squares, circles, and upward- and downward-pointing triangles are from Ho (2009), Greene & Ho (2007), Kauffmann & Heckman (2009), and Heckman et al. (2004), respectively, which are all compiled from low-redshift observations.

only the “runaway stars” would be visible to distant observers. Of course, after the outbursts when the dust clears, an A-type spectrum would be seen from stars distributed as shown in Figure 7.

In Figure 9, we plot the dust optical depth for the UV photons from the AGN (see Equation (21)) at redshift zero, where the UV optical depth is integrated along radial directions with fixed θ , since the AGN can be treated as a point source. Comparing to the lower-left panel of Figure 3, we find that most of the dusty disk is optically thick to the UV photons from the central AGN, i.e., all of the AGN emission is obscured behind the circumnuclear disk. The solid angle of the dusty disk is ~ 2.36 sr, i.e., the covering factor is $\sim 19\%$ of the 4π solid angle.

6.2. Dust Thermodynamics

In this section, we describe how we derive the infrared emission of dust from the simulation outputs. Following Hensley et al. (2014), we assume the dust emission in infrared is in equilibrium with its heating processes, i.e.,

$$P_{\text{dust}}^{\text{IR}} \equiv \sigma T_{\text{dust}}^4 \int_{a_{\text{min}}}^{a_{\text{max}}} da \frac{dn_d}{da} \cdot 4\pi a^2 \bar{Q}(a, T_{\text{dust}}) = H_{\text{dust,abs}}^{\text{rad}} + H_{\text{dust,collision}}^{\text{gas}} \quad (29)$$

where $P_{\text{dust}}^{\text{IR}}$ is the dust emission power per unit volume, T_{dust} is the dust temperature, and $\bar{Q}(a, T_{\text{dust}})$ is the Planck-averaged emission efficiency (see Hensley et al. 2014, their Equation (33), where the Planck-averaged absorption cross sections for silicate grains are used; see also Schurer et al. 2009; Draine 2011). Therefore, provided the heating terms, the dust temperature can be calculated according to the equation above.

The heating sources are mainly contributed to by collisional heating $H_{\text{dust,collision}}^{\text{gas}}$ and radiative heating $H_{\text{dust,abs}}^{\text{rad}}$. The collisional heating is calculated according to Equation (18), and assumes equilibrium when the cooling timescale is short as in the hydrodynamical part of the simulation. Unfortunately, the assessment of the radiative heating of dust is much more complicated—there are two radiative heating sources for the

dust grains, i.e., the AGN radiation and the stellar radiation,

$$H_{\text{dust,abs}}^{\text{rad}} = H_{\text{dust,abs}}^{\text{AGN}} + H_{\text{dust,abs}}^{\text{stars}} \quad (30)$$

The dust heating by AGN irradiation $H_{\text{dust,abs}}^{\text{AGN}}$ is calculated similarly to Equations (20) and (21), but with both the UV and optical photons. However, one can not assess $H_{\text{dust,abs}}^{\text{stars}}$ self-consistently without including sophisticated radiative transfer, and the latter is extremely computationally expensive. Fortunately, we find that the dust is usually optically thick to the local stellar radiation of the new stars, which makes it possible to allow for some simplification, i.e., we estimate $H_{\text{dust,abs}}^{\text{stars}}$ directly with the local stellar radiation from the new stars $\dot{E}_{\text{*,rad}}^+$, assuming that all of the local stellar radiation is absorbed by dust.

$$H_{\text{dust,abs}}^{\text{stars}} \sim \dot{E}_{\text{*,rad}}^+ \sim \dot{E}_{\text{*,UV}}^+ + \dot{E}_{\text{*,opt}}^+, \quad (31)$$

where the stellar radiation of the new stars is mainly in the UV ($\dot{E}_{\text{*,UV}}^+$) and optical ($\dot{E}_{\text{*,opt}}^+$) bands.

Following Ciotti & Ostriker (2012), we compute the UV and optical luminosity per unit volume of the new stars according to the star formation history,

$$\dot{E}_{\text{*,UV}}^+ = \frac{\epsilon_{\text{UV}} c^2}{t_{\text{UV}}} \int_0^t \dot{\rho}_{\text{*}}^+(t') \cdot e^{-\frac{t-t'}{t_{\text{UV}}}} dt', \quad (32)$$

$$\dot{E}_{\text{*,opt}}^+ = \frac{\epsilon_{\text{opt}} c^2}{t_{\text{opt}}} \int_0^t \dot{\rho}_{\text{*}}^+(t') \cdot e^{-\frac{t-t'}{t_{\text{opt}}}} dt', \quad (33)$$

where $\dot{\rho}_{\text{*}}^+$ is the star formation rate density (which is given by the MACER simulations). In the equations above, $\epsilon_{\text{opt}} = 1.24 \times 10^{-3}$, $\epsilon_{\text{UV}} = 8.65 \times 10^{-5}$, $t_{\text{opt}} = 1.54 \times 10^8$ yr, $t_{\text{UV}} = 2.56 \times 10^6$ yr are the efficiency and characteristic time of optical and UV emission, respectively.

Note that we ignore the dust opacity of the infrared emission itself in the calculations above, which could be important in the near or mid-near-infrared band (Hönig 2019), and we leave it for future work.

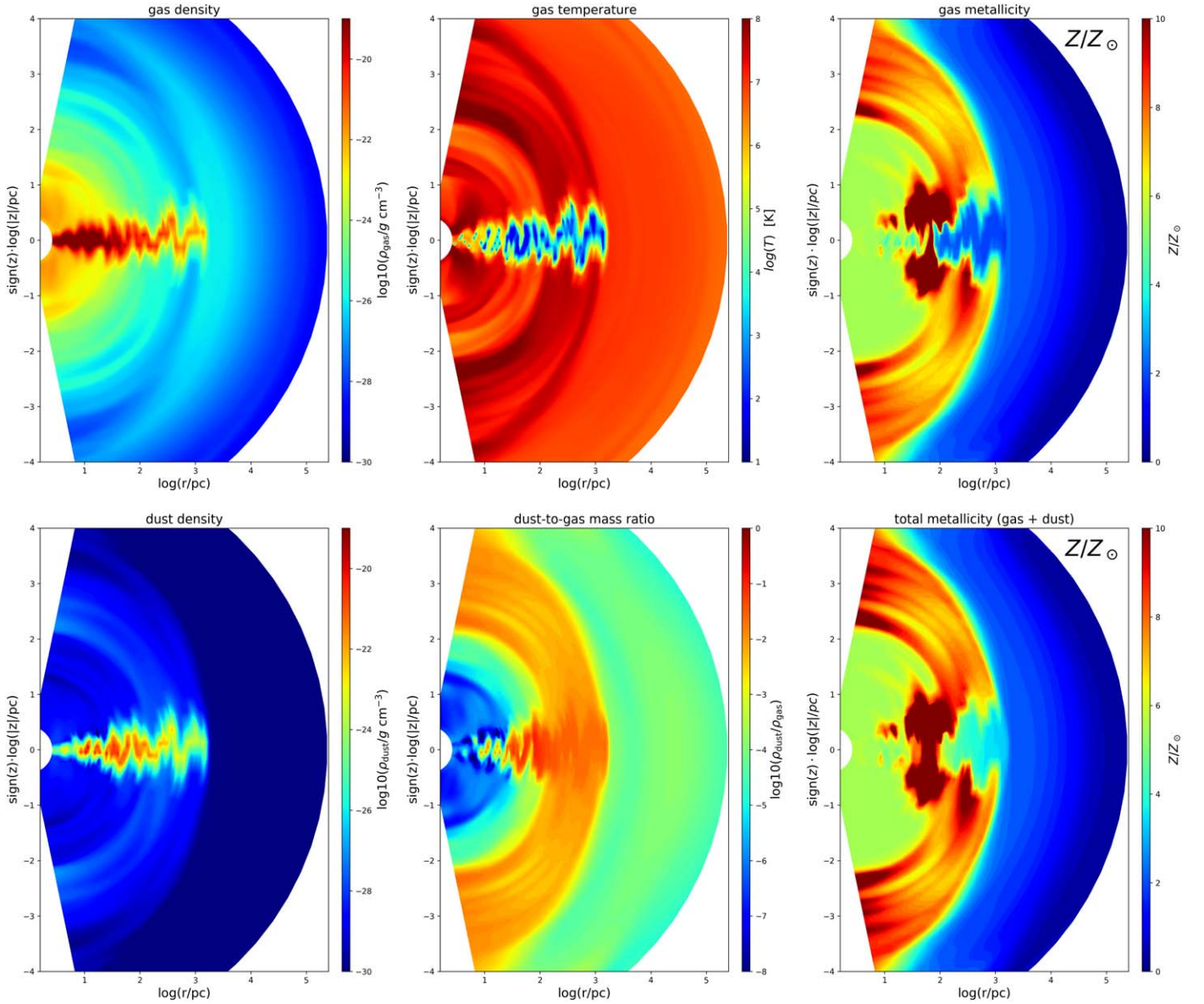


Figure 3. Hydrodynamical properties of the cold gas dusty circumnuclear disk at the end of the simulation, showing the gas density, gas temperature, gas metallicity, dust density, dust-to-gas mass ratio, and the total metallicity, respectively. Note the logarithmic radial scale.

6.3. Infrared Emission

In Figure 10, we present the results from the data post-processing of the dust infrared emission. In the calculation, we assume the gas and dust are transparent to the infrared photons; therefore, the total infrared luminosity L_{TIR} of the galaxy is simply the sum of the dust infrared emission in each cell, making it possible to assess the contributions of dust emission by the AGN irradiation, starlight, and dust–gas collisional heating, separately (in the upper panels, (a) and (b), of Figure 10). In the lower panels, (c) and (d), we present the total infrared luminosity (black line).

In Figure 11, we plot the spatial distribution of the dust emission during the AGN outburst at $t = 2.44$ Gyr. It shows that the dust emission during the outbursts is mostly due to the AGN irradiation of the innermost region and the surface of the disk where the optical depth to the central AGN is not obscured. As other evidence, in the bottom panel of Figure 12, we plot the scatter of the half-light radius of the dust infrared

emission versus the total infrared luminosity. We can see that the half-light radius decreases moderately when the infrared luminosity increases, with typical values of approximately 30 pc at 2×10^{44} erg s $^{-1}$. In the top panel of Figure 12, we plot the scatter of the infrared emission weighted dust temperature versus the total infrared luminosity, where a tight correlation is found. While most of the gas mass is in the X-ray emitting, extended hot component, most of the infrared radiation is emitted by the highly concentrated cold component.

In Figure 13, we present the histogram of infrared luminosity in dust temperature bins, in which the vertical axis is the total instantaneous infrared luminosity integrated over the galaxy within a given dust temperature bin. The colored lines are the results from three representative time snapshots, i.e., $t = 2.44$ Gyr during an AGN burst without starburst; $t = 4.13$ Gyr without AGN burst while with starburst; and $t = 9.39$ Gyr when the galaxy is quiescent, respectively (see also the samples in Figure 12 for more details). We can see that the dust temperature peaks around $\sim 10^2$ K, and it is systematically higher when the infrared

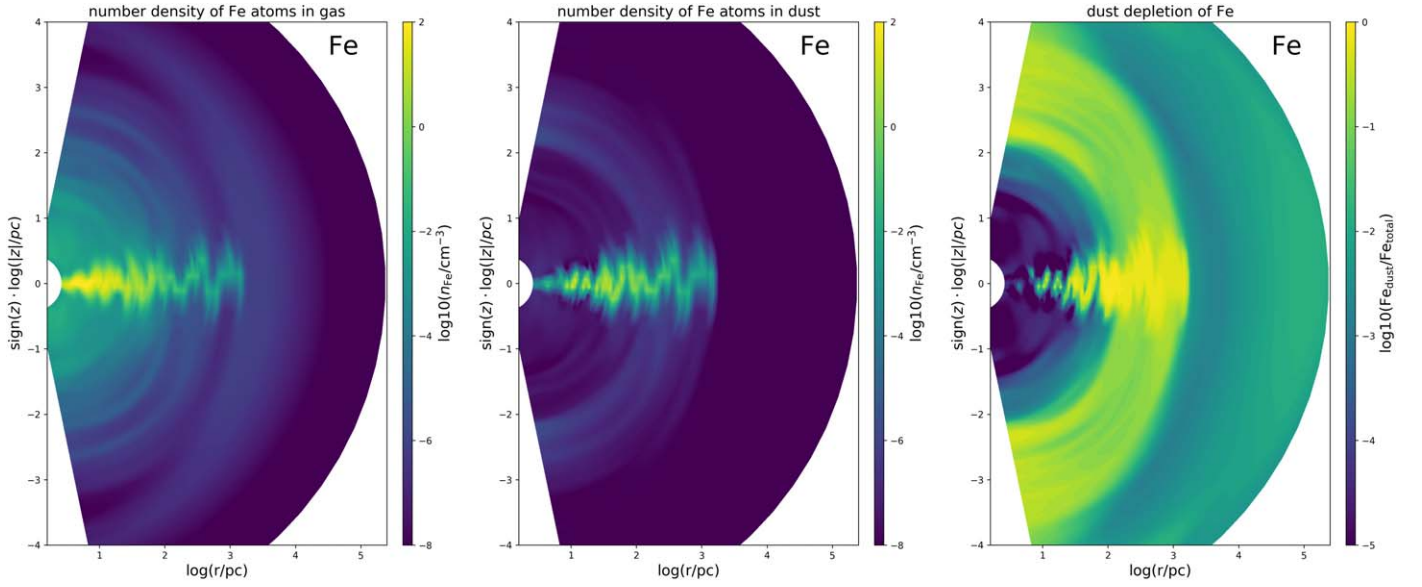


Figure 4. Dust distribution and depletion of Fe at the end of the simulation. Note the logarithmic radial scale.

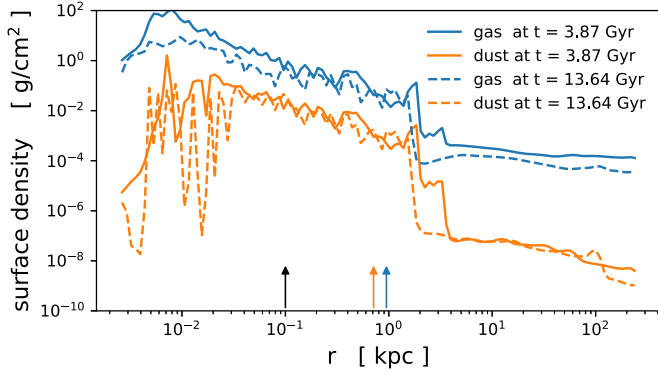


Figure 5. Surface density of the gas and dust component in the circumnuclear disk at the end of the simulation. The vertical black arrow indicates the radius of influence of the central black hole within which it dominates the gravitational potential. The vertical orange and blue arrows indicate the half-mass-radius of the dust disk and that of the cold/warm gas ($T_e < 10^5$ K) disk, respectively.

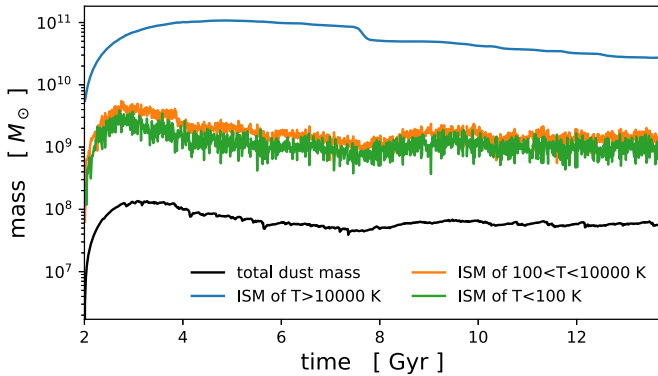


Figure 6. Total mass of dust grains and gaseous ISM in different ranges of temperature. As expected, hot X-ray emitting gas dominates.

luminosity increases, especially during the AGN outbursts when the dust heating is dominated by the AGN irradiation. The dust temperature can reach ~ 500 K in the innermost region near the

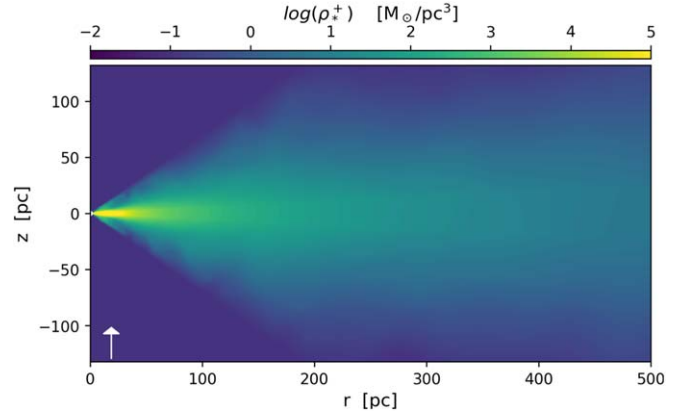


Figure 7. The cumulative star formation (stellar mass density) in the circumnuclear disk at the end of the simulation. The half-mass-radius is ~ 20 pc as indicated by the vertical arrow.

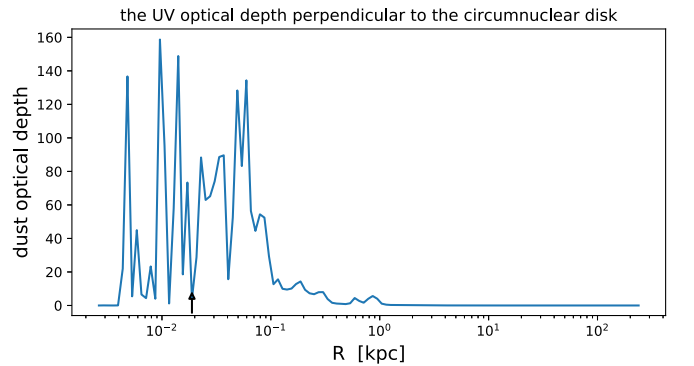


Figure 8. Dust optical depth in the UV band perpendicular to the circumnuclear disk during the starburst at $t_{\text{age}} = 4.13$ Gyr. The vertical arrow is at the half-mass-radius of the new stars.

central AGN, while the typical dust temperature in the circumnuclear disk is ~ 30 K.

In Figure 14, we present the duty cycle of the infrared luminosity from dust, i.e., the fraction of time when the infrared luminosity is above the given values. It shows that most of time

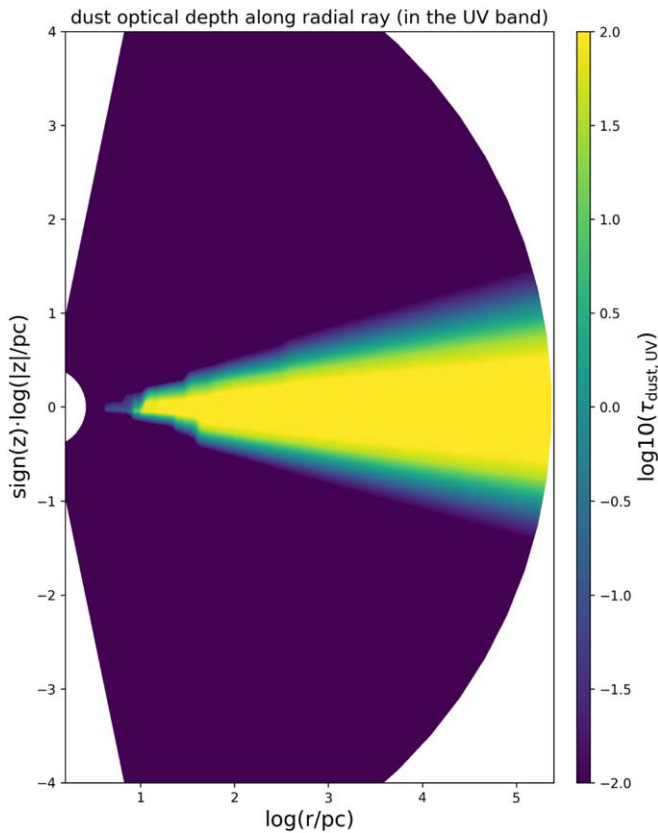


Figure 9. Dust optical depth at the end of the simulation in the UV band along radial directions from the center. Note the logarithmic radial scale.

the infrared luminosity is $>3 \times 10^{43} \text{ erg s}^{-1}$, and it systematically decreases when the redshift decreases. The median value is $\sim 2 \times 10^{44} \text{ erg s}^{-1}$ (the blue line), or $\sim 1/2$ of that at late times (the red line).

In Figure 15, we plot the histograms of the dust infrared emission. It shows that there is a clear redshift dependency of the dust infrared luminosity, i.e., the infrared luminosity decreases systematically as the redshift decreases. Again, this is due to the AGN irradiation (which contributes the most energy for dust emission), as there is more AGN activity at high redshift (see also Figures 1 and 2). In all of the histograms, we can also see a cutoff around the infrared luminosity $\sim 3 \times 10^{43} \text{ erg s}^{-1}$. We find in the simulation that the collisions between dust grains and the gaseous medium always contribute significant infrared emission, no matter whether there are AGN bursts and/or star formation, though the latter may boost the dust collisional heating via feedback processes. As a consequence, there is a “floor” luminosity due to the collisional heating ($\sim 10^{43} \text{ erg s}^{-1}$ in our simulated galaxy; see the green line in the top panel of Figure 10), which results in the cutoff in the histogram. The stellar irradiation by the embedded new stars also contributes a significant fraction of the energy for the dust infrared emission (see the orange line in the top panel of Figure 10).

6.4. Dependence on Initial Conditions and Resolution

In this subsection, we study the dependence of our results on the initial conditions and spatial resolution.

In the fiducial model, we have adopted the previously standard assumption that, after formation, elliptical galaxies have a low gas fraction, and so for simplicity, we took a gas-free initial state with all subsequent gas content due to cosmological infall or mass loss from evolving stars. This fiducial model is the “high-res” model in Table 3, and it has an inner boundary of 2.5 pc. To determine the importance of our high spatial resolution, we include, as the “low-res” model, a simulation that is identical except for an inner boundary of 25 pc, which is still small compared to the resolution of most cosmological simulations.

We see some dramatic changes in the lower-resolution model. The infrared luminosity is much higher, and the dusty disk is much smaller in the high-resolution model. Additionally, the new stars are much more numerous and concentrated when resolution is increased. The black hole final mass is less of a consequence, since the gas flowing in toward the center can be turned into stars before reaching the central black hole.

The implication is strong that a still higher spatial resolution (currently beyond technical reach) would further enhance these trends. It is possible however that heating from the central black hole would limit star formation within, as we see in Figure 3, $r < 10 \text{ pc}$.

The other variation on our fiducial model is based on starting the simulation with a gas/star ratio of 30%, close to the value seen in the recent ALMA/SCUAB-2 survey of submillimeter galaxies (Dudzevičiūtė et al. 2020). That work (see their Figure 11(d)) indicates a gas/star ratio of roughly 20%–40% at redshift $z = 2$. To save computer time, we ran the simulation with 30% initial gas fraction, which was identical to the low-resolution model “low-res,” labeling the high initial gas model “low-res+gas” in Table 3. We see several important changes. First, it is much more “bursty” with 37% of the AGN radiation energy emitted above $L/L_{\text{Edd}} = 0.1$. As expected, there is more star formation, more infrared emission, and a higher X-ray luminosity.

Figure 15 shows the distribution of infrared luminosities for the three simulations as a function of redshift range. Both higher resolution and more initial gas push up the infrared luminosities to $10^{44} \text{ erg s}^{-1}$ at late times and $10^{45} \text{ erg s}^{-1}$ at redshift above $z = 2$.

A model with both higher resolution and more initial gas is being studied and will be reported in a subsequent communication.

7. Comparison to Observations

While earlier 1D models incorporating the grain physics have already been compared to observations in Hensley et al. (2014; previous attempts to model the dust emission and its SED can be also found in Schurer et al. 2009), the current 2D models allow for a more detailed comparison across redshift and galaxy properties. The existence of cold gas rotating disks in the more realistic 2D models greatly enhances IR emission.

7.1. High Redshift

Extending to high redshift, Schreiber et al. (2018) fit models to stacked SEDs from deep CANDELS fields, including stacked Herschel and ALMA data. Although their model templates applied to the observations do not include emission from a dusty AGN torus, this should have little impact on their derived L_{TIR} and stellar masses. For their highest stellar mass

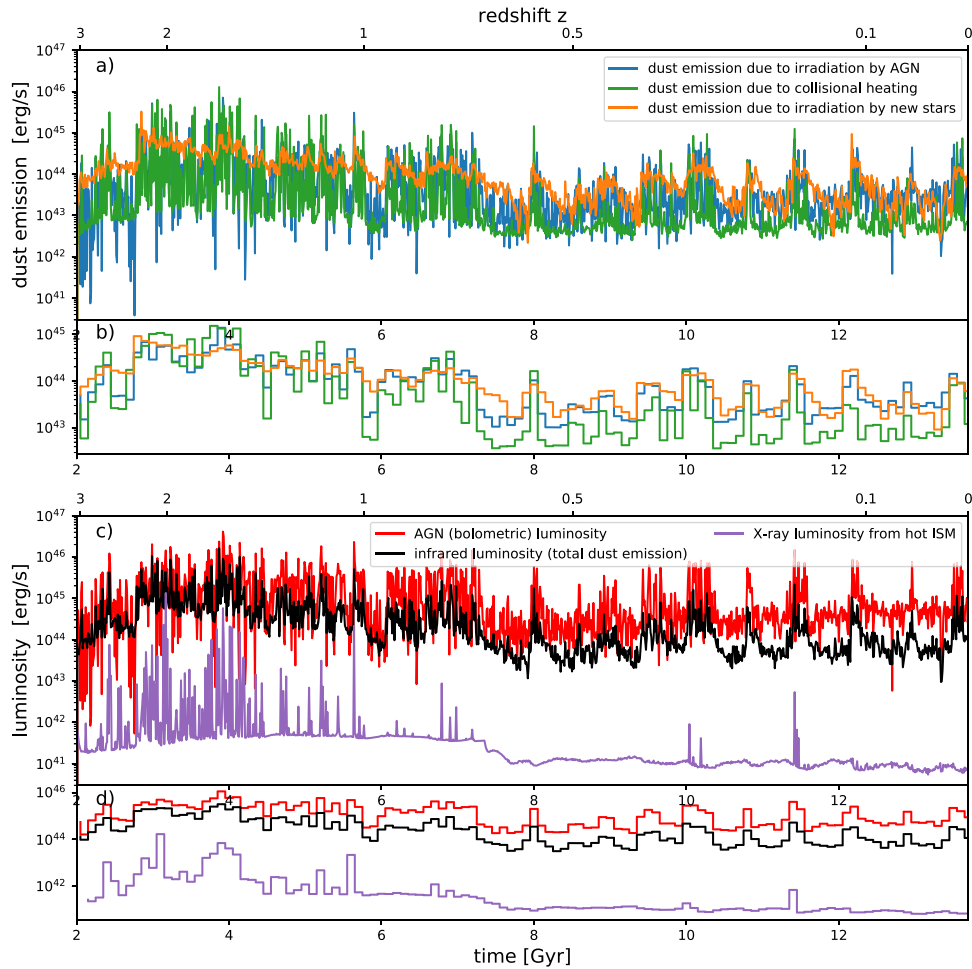


Figure 10. Infrared emission from dust. A rough estimate of the wavelength of the infrared emission can be found by considering Figure 12 (top panel), which shows a strong correlation between dust temperature and luminosity. The time resolution in panels (a) and (c) is $\sim 10^7$ yr, while panels (b) and (d) average over a 10^8 yr timescale.

bin ($11 < \log M_* < 11.5$), both data and models suggest stacked-average $L_{\text{TIR}} \sim 3, 7, 17, 29,$ and $51 \times 10^{44} \text{ erg s}^{-1}$ at $z \sim 0.5, 1, 1.5, 2.2,$ and 3 , respectively. These L_{TIR} values are in excellent agreement with our predictions (see Figure 15).

Such high-luminosity massive galaxies are likely to evolve into the quiescent massive galaxies observed in the local universe. For example, using ALMA, Wang et al. (2019) recently discovered a population of very massive, optically faint, IR-luminous galaxies at $z \sim 4$ with average $L_{\text{TIR}} = 40 \times 10^{44} \text{ erg s}^{-1}$. This population has a clustering/bias factor consistent with the population expected to be the progenitors of massive galaxies in groups and clusters in the local universe, such as the one modeled here.

Results from Schreiber et al. (2018) suggest that at $z > 1$, massive galaxies dominate the luminous end of the total infrared (TIR) luminosity function (LF). Our model suggests high IR variability with a broad, flattened distribution over $\log L_{\text{TIR}}$. Measurements of the TIR (or far-IR) LF (e.g., Gruppioni et al. 2013; Koprowski et al. 2017) are relatively consistent with the range and shape of the distribution we infer. However these LFs are themselves discrepant on the bright end, possibly due to differing selection effects with respect to AGNs or galaxies with a warmer dust component (see, e.g., Gruppioni & Pozzi 2019).

7.2. Low Redshift

At low redshifts, for $z < 0.5$, our model predicts a median infrared luminosity $\sim 1.2 \times 10^{44} \text{ erg s}^{-1}$, and 90% of the time, $L_{\text{TIR}} < 4 \times 10^{44} \text{ erg s}^{-1}$ (see Figure 14). While luminosities fall just below the lower bound for the typical definition of luminous infrared galaxies, these luminosities are nevertheless comparable or even higher than those of less-massive star-forming galaxies. There is evidence that some relatively quiescent massive galaxies have TIR luminosities in this range.

Andreani et al. (2018) measured the bivariate luminosity and mass functions from a local sample from the Herschel Reference Survey. For galaxies with high stellar masses (e.g., $\log M_* > 11.5$), their bivariate function implies a broad range of TIR luminosities centered on $(1\text{--}2) \times 10^{43} \text{ erg s}^{-1}$. Their analysis only includes galaxies classified as late-types, but the massive galaxies included in their analysis are likely to contain a significant spheroidal component.

Surveys of IR emission from dust in early-types in the nearby universe typically contain only a handful of galaxies with high stellar masses ($\log M_* > 11$). Amblard et al. (2014) extract physical properties from 221 early-type galaxies of which ~ 50 have high stellar masses. The median L_{dust} of this subsample is $10^{42} \text{ erg s}^{-1}$, with five (10%) above $10^{43} \text{ erg s}^{-1}$. Infrared AKARI observations of 260 early-type galaxies in the

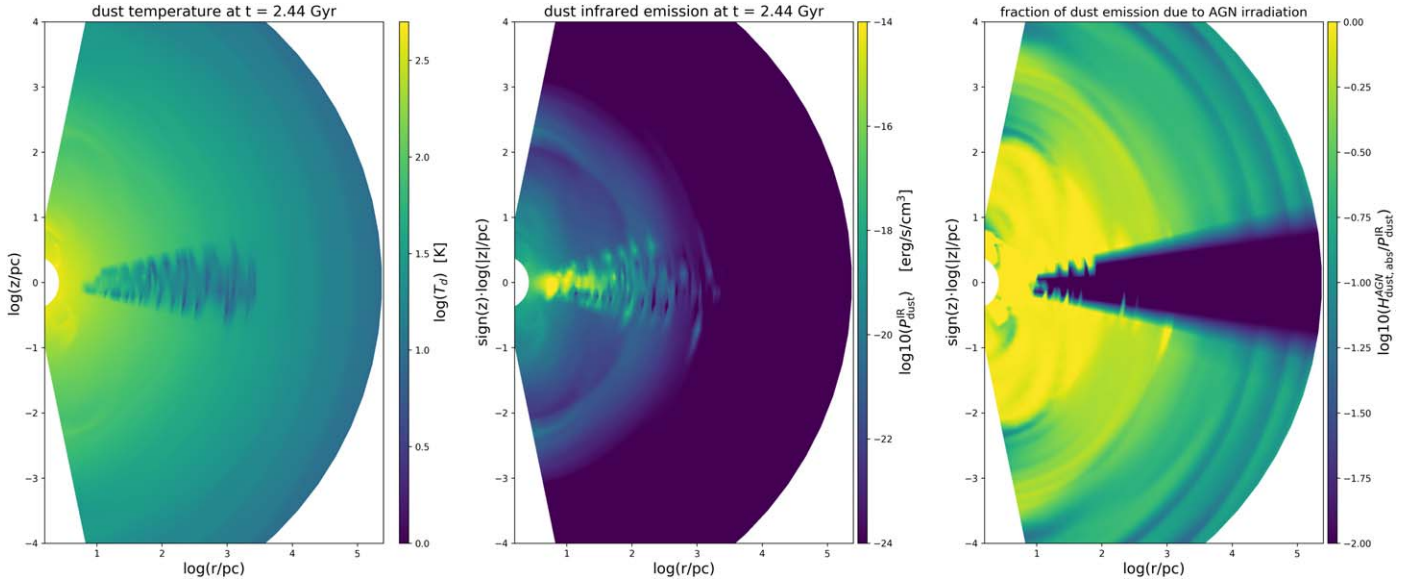


Figure 11. Dust temperature (left panel), its infrared emission power per unit volume (middle panel), and the fraction of the dust emission due to AGN irradiation (right panel) during the outburst at $t = 2.44$ Gyr, when the AGN output is $0.08L_{\text{edd}}$, the star formation rate is $1.7M_{\odot} \text{ yr}^{-1}$, and the total infrared luminosity $L_{\text{TIR}} = 7.4 \times 10^{44} \text{ erg s}^{-1}$. Note the logarithmic radial scale.

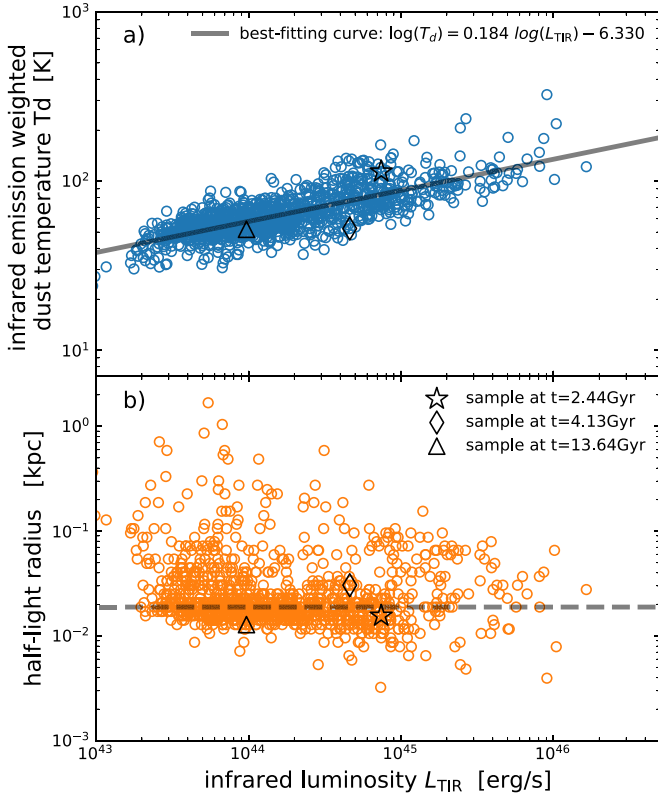


Figure 12. Top panel: infrared emission weighted dust temperature. We can see a strong correlation between dust temperature and luminosity, which also makes it possible to obtain a rough estimate of the wavelength of the infrared emission. The empty circles are the data sampled for every 10 Myr throughout the whole simulation. The black solid line is our best-fitting curve. Bottom panel: half-light radius of the dust infrared emission. The dashed line shows the median size of 20 pc.

Atlas3D sample (Kokusho et al. 2017, 2019) do include several tens of high-mass galaxies, with a spread of L_{TIR} in the 10^{42} – $10^{43} \text{ erg s}^{-1}$ range, and occasionally higher. Interestingly, they note much wider scatter in warm dust luminosities (at a

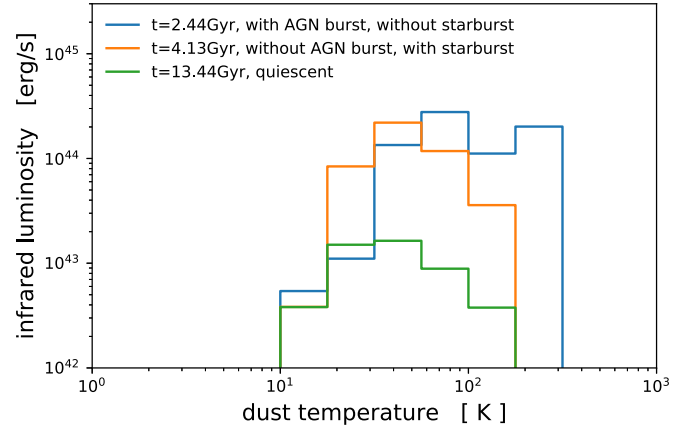


Figure 13. Histogram of infrared luminosity in dust temperature bins. The vertical axis is the total instantaneous infrared luminosity integrated over the galaxy within a given dust temperature bin.

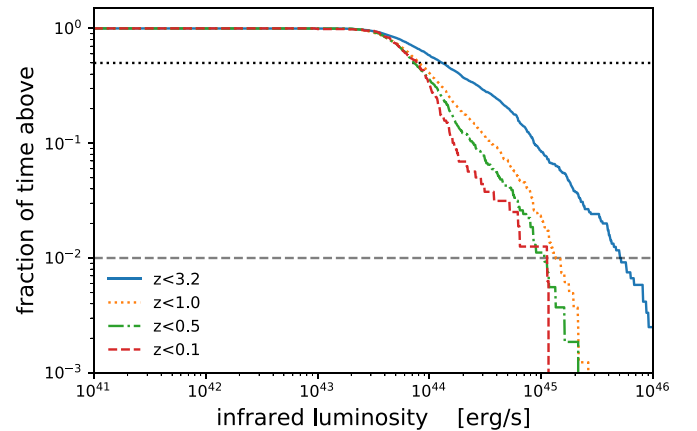


Figure 14. Duty cycle of the infrared luminosity from dust, i.e., the fraction of time when the infrared luminosity is above the given values. The horizontal dotted line is at the 50% level and dashed at the 1% level.

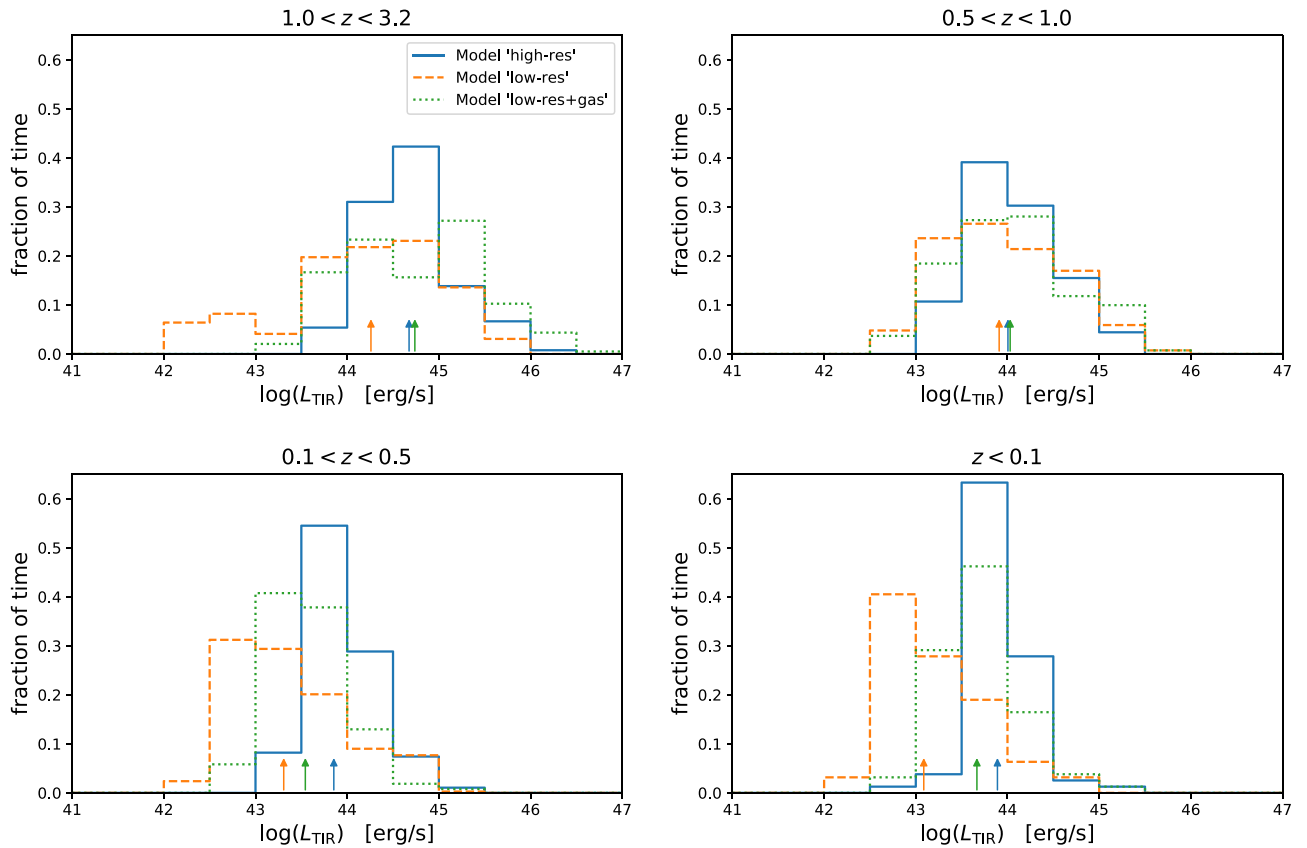


Figure 15. Histogram of infrared luminosity from dust. The vertical arrows indicate the median values of the infrared luminosity.

fixed stellar mass), and they conclude that this is likely due to variation in AGN activity across the sample. Galaxies with dusty nuclei and/or post-starburst signatures also show high IR luminosities. For example, in a sample of E+A galaxies, Smercina et al. (2018) measure $L_{\text{TIR}} \sim 10^{43.5}$ and 10^{44} erg s^{-1} for two galaxies with high stellar mass.

8. Conclusions and Discussions

We have developed the MACER code for exploring the evolution of massive elliptical galaxies at a high spatial resolution down to and within the fiducial Bondi radius. Though it is still a 2D code, the high time and spatial resolution enable us to study the coevolution between the supermassive black holes and their host galaxies self-consistently, which is difficult for large-scale cosmological simulations. In our hydrodynamical simulations, we have included a relatively complete set of stellar physics, galaxy dynamics, and AGN feedback processes. In the presence of significant rotation, circumnuclear disks form in the center of elliptical galaxies, which is a natural consequence of standard cooling flows, but the mass inflow is obstructed because of its angular momentum barrier (Gan et al. 2019b). The circumnuclear disk is found to be cold and dense with a typical mass of $10^9 M_{\odot}$, which makes it an ideal site for star formation when it becomes self-gravitating. The latter also permits angular momentum transfer and thus allows mass inflow onto the central supermassive black hole (after some time lag). Therefore, one can always expect a near coincidence between star formation and AGN activities (with rates even exceeding those of spiral galaxies), though we found in the simulations that in most of their lifetime, the simulated galaxies are stereotypical “quiescent” elliptical galaxies.

In our previous paper (Gan et al. 2019a), we added a suite of chemical abundances into the MACER code to track the metal enrichment due to the passive stellar evolution of AGB stars and SNe Ia and II. However, we did not consider dust grains, which are known to be important in depleting metals. Especially in the circumnuclear disk, the cold and dense environment favors dust grain growth. Therefore, a dusty disk can be expected, and it can also be important in absorbing the starlight within the disk and in obscuring the AGN radiation from the galaxy center. Such dusty disks are by now well observed. The computed infrared emission from the dust may also provide a diagnosis to test our model observationally.

Following Hensley et al. (2014), we implement the following grain physics into our code (assuming dust grains co-move with the gaseous ISM): (a) dust grains made and injected in the passive stellar evolution; we assume that most of the metals in the stellar ejecta are in dust grains; (b) dust grain growth due to collision and sticking; (c) dust grain destruction due to thermal sputtering; (d) dust cooling of hot gas via inelastic collisions; and (e) radiation pressure on dust grains.

The representative galaxy model adopted for the simulation has a stellar mass of $6.1 \times 10^{11} M_{\odot}$, a central stellar velocity dispersion of ~ 260 km s^{-1} , and ellipticity 0.37. We studied the time evolution of the dust, including its spatial distribution, its depletion of metals, its absorption of the starlight within the circumnuclear disk, its obscuration of the central AGN radiation, and finally its infrared emission. We find that:

1. In more than half ($\sim 55\%$) of its lifetime, the simulated galaxy is a stereotypical “quiescent” elliptical galaxy with little star formation ($\lesssim 2 M_{\odot} \text{ yr}^{-1}$). However, during the central outbursts, the star formation rate can be up to

Table 3
Simulation Outputs of the Model Galaxy^a

Model	AGN Duty Cycle ^b			M_{BH}^c ($10^9 M_{\odot}$)	SF ^d ($10^9 M_{\odot}$)	$\langle \text{SFR} \rangle^e$ ($M_{\odot} \text{ yr}^{-1}$)	$\langle L_X \rangle^{f,1}$ ($10^{42} \text{ erg s}^{-1}$)	$\langle R_{0.5}^X \rangle^g$ (kpc)	$\langle L_{\text{TIR}} \rangle^h$ ($10^{43} \text{ erg s}^{-1}$)	$\langle R_{0.5}^{\text{IR}} \rangle^i$ (kpc)	$\langle M_{\text{gas}}^{\text{cold}} \rangle^j$ ($10^9 M_{\odot}$)	R_{disk}^k (kpc)
	$f_{l>0.1}$	$l_{\text{median}}^{\text{energy}}$	$l_{\text{median}}^{\text{time}}$									
high-res	7.62%	0.011	0.00094	6.72	32.9	1.24	0.07	14.5	8.23	0.03	0.97	1.53
low-res	9.59%	0.025	0.00042	8.32	9.84	0.15	0.10	31.6	1.60	0.41	2.05	1.52
low-res+gas	37.0%	0.039	0.00026	25.6	26.4	0.33	0.33	19.5	5.39	0.40	3.06	1.67

Notes.

^a From left to right, the columns in the table above present the simulation results as follows:

^b AGN duty cycle, including the percentage of the cumulative radiation energy that the AGN emits when its Eddington ratio $l \equiv L_{\text{AGN}}/L_{\text{Edd}}$ is above 0.1 (i.e., $f_{l>0.1}$), the median Eddington ratio above which the AGN emits half of its total energy (i.e., $l_{\text{median}}^{\text{energy}}$), and the median Eddington ratio above which the AGN spends half of the simulated cosmological time span (i.e., $l_{\text{median}}^{\text{time}}$).

^c the final black hole mass M_{BH} (the initial black hole is $0.61 \times 10^9 M_{\odot}$ in all simulations).

^d total star formation.

^e averaged star formation rate ($\langle \text{SFR} \rangle$).

^f averaged X-ray luminosity from the hot ISM ($\langle L_X \rangle$).

^g averaged half-light radius of the X-ray emission ($\langle R_{0.5, X} \rangle$).

^h averaged infrared luminosity from dust ($\langle L_{\text{TIR}} \rangle$).

ⁱ averaged half-light radius of the infrared emission ($\langle R_{0.5, \text{IR}} \rangle$).

^j averaged mass of the cold gas with temperature lower than 100 K ($\langle M_{\text{gas}}^{\text{cold}} \rangle$).

^k size of the circumnuclear disk at the end of the simulations (R_{disk}).

^l All of the averages are made using the simulation data in the last 1 Gyr.

$>250 M_{\odot} \text{ yr}^{-1}$. All star formation occurs within the circumnuclear disk, which is optically thick. The size of the disk is ~ 1 kpc, while the half-mass-radius of the resulting stars is of the order of 20 pc.

2. It is dusty in the outer disk ($r \sim 1$ kpc) where most of the metals are in dust grains, while in the inner disk ($r \lesssim 20$ pc), most of the dust grains are destroyed by thermal sputtering in the hot, AGN-irradiated gas.
3. The dusty disk is optically thick to both the starlight within the disk and the radiation from the central AGN. The AGN is expected to be obscured behind the circumnuclear disk, having a covering factor of ~ 0.2 .
4. The total infrared radiation from the dust is greater than the X-rays from the hot gas. The median infrared luminosity from the dust is $\sim 2 \times 10^{44} \text{ erg s}^{-1}$, and it can reach up to $\sim 10^{46} \text{ erg s}^{-1}$ during outbursts. Most of the dust infrared emission is due to the AGN irradiation, and it is located at the innermost region and on the surface of the dusty disk where the dust optical depth is moderate compared to the AGN radiation. The half-light radius of the infrared emitting region is ~ 30 pc during bursts.

One test of our modeling could come from the measurement of half-light radii (R_e). In the X-ray regions, typical sizes are computed to be ~ 100 kpc. In the optical (by assumption), the half-light radius is ~ 10 kpc. It is striking that our computed infrared sizes are typically much smaller (30 pc), and this prediction should be able to be tested by the James Webb Space Telescope.

For future work, we also plan to extend our simulations into three dimensions. Our current treatments for some important physics processes are limited by the 2D settings. For example, the assumption of axial symmetry breaks down in the Toomre instability, which is intrinsically 3D—it is extremely important to both AGN feeding and star formation. It is also true for supernova explosions, in our current 2D settings, that we have to average the SN-ISM energy coupling in the axial direction, i.e., the SN heating is averaged over rings, rather than

disposing its energy locally, where the latter would induce more anisotropy to the X-ray emitting ISM as observed.

We thank David Spergel and the Center for Computational Astrophysics for generous support of this work and also James Stone and Princeton University for their generous support as well. We thank Jeremy Goodman, James Stone, Kengo Tomida, Pieter van Dokkum, Nadia Zakamska, Takayuki Saitoh, Tuguldur Sukhboldfor, Charlie Conroy, Feng Yuan, and Doosoo Yoon for useful discussions. We thank Gregory S. Novak for sharing the first 2D version of the MACER code in 2011, which was using ZEUSMP/1.5. We acknowledge computing resources from Columbia University's Shared Research Computing Facility project, which is supported by NIH Research Facility Improvement grant 1G20RR030893-01, and associated funds from the New York State Empire State Development, Division of Science Technology and Innovation (NYSTAR) Contract C090171, both awarded 2010 April 15. We are also pleased to acknowledge that the work reported in this paper was substantially performed using the Princeton Research Computing resources at Princeton University, which is a consortium of groups including the Princeton Institute for Computational Science and Engineering and the Princeton University Office of Information Technology's Research Computing department.

ORCID iDs

Zhaoming Gan  <https://orcid.org/0000-0003-3886-0383>
 Brandon S. Hensley  <https://orcid.org/0000-0001-7449-4638>
 Jeremiah P. Ostriker  <https://orcid.org/0000-0002-6405-9904>
 Luca Ciotti  <https://orcid.org/0000-0002-5708-5274>
 Silvia Pellegrini  <https://orcid.org/0000-0002-8974-2996>

References

Amblard, A., Riguccini, L., Temi, P., et al. 2014, *ApJ*, 783, 135
 Andreani, P., Boselli, A., Ciesla, L., et al. 2018, *A&A*, 617, A33

- Arav, N., Borguet, B., Chamberlain, C., Edmonds, D., & Danforth, C. 2013, *MNRAS*, **436**, 3286
- Arav, N., Liu, G., Xu, X., et al. 2018, *ApJ*, **857**, 60
- Asplund, M., Grevesse, N., Sauval, A. J., & Scott, P. 2009, *ARA&A*, **47**, 481
- Balbus, S. A., & Hawley, J. F. 1998, *RvMP*, **70**, 1
- Bartko, H., Martins, F., Trippe, S., et al. 2010, *ApJ*, **708**, 834
- Bentz, M. C., & Manne-Nicholas, E. 2018, *ApJ*, **864**, 146
- Bertin, G., & Lodato, G. 1999, *A&A*, **350**, 694
- Boizelle, B. D., Barth, A. J., Darling, J., et al. 2017, *ApJ*, **845**, 170
- Brennan, R., Choi, E., Somerville, R. S., et al. 2018, *ApJ*, **860**, 14
- Burkhart, B., & Mocz, P. 2019, *ApJ*, **879**, 129
- Calura, F., Pipino, A., & Matteucci, F. 2008, *A&A*, **479**, 669
- Calzetti, D., Lee, J. C., Sabbi, E., et al. 2015, *AJ*, **149**, 51
- Choi, E., Ostriker, J. P., Naab, T., et al. 2017, *ApJ*, **844**, 31
- Ciotti, L., & Ostriker, J. P. 1997, *ApJL*, **487**, L105
- Ciotti, L., & Ostriker, J. P. 2012, in *Hot Interstellar Matter in Elliptical Galaxies*, Astrophysics and Space Science Library, Vol. 378, ed. D.-W. Kim & S. Pellegrini (New York: Springer), **83**
- Davis, T. A., Alatalo, K., Sarzi, M., et al. 2011, *MNRAS*, **417**, 882
- Davis, T. A., Young, L. M., Crocker, A. F., et al. 2014, *MNRAS*, **444**, 3427
- Draine, B. T. 2011, *Physics of the Interstellar and Intergalactic Medium* (Princeton, NJ: Princeton Univ. Press)
- Draine, B. T., & Lee, H. M. 1984, *ApJ*, **285**, 89
- Draine, B. T., & Salpeter, E. E. 1979, *ApJ*, **231**, 77
- Dudzevičiūtė, U., Smail, I., Swinbank, A. M., et al. 2020, *MNRAS*, **494**, 3828
- Eisenreich, M., Naab, T., Choi, E., Ostriker, J. P., & Emsellem, E. 2017, *MNRAS*, **468**, 751
- Eldridge, J. J., Langer, N., & Tout, C. A. 2011, *MNRAS*, **414**, 3501
- Frazer, C. C., & Heitsch, F. 2019, *MNRAS*, **489**, 52
- Gall, C., Andersen, A. C., & Hjorth, J. 2011, *A&A*, **528**, A13
- Gan, Z., Choi, E., Ostriker, J. P., Ciotti, L., & Pellegrini, S. 2019a, *ApJ*, **875**, 109
- Gan, Z., Ciotti, L., Ostriker, J. P., & Yuan, F. 2019b, *ApJ*, **872**, 167
- Goodman, J. 2003, *MNRAS*, **339**, 937
- Goodman, J., & Tan, J. C. 2004, *ApJ*, **608**, 108
- Greene, J. E., & Ho, L. C. 2007, *ApJ*, **667**, 131
- Gruppioni, C., & Pozzi, F. 2019, *MNRAS*, **483**, 1993
- Gruppioni, C., Pozzi, F., Rodighiero, G., et al. 2013, *MNRAS*, **432**, 23
- Heckman, T. M., Kauffmann, G., Brinchmann, J., et al. 2004, *ApJ*, **613**, 109
- Hensley, B. S., Ostriker, J. P., & Ciotti, L. 2014, *ApJ*, **789**, 78
- Ho, L. C. 2009, *ApJ*, **699**, 638
- Hönig, S. F. 2019, *ApJ*, **884**, 171
- Hopkins, P. F., Wetzell, A., Kereš, D., et al. 2018, *MNRAS*, **480**, 800
- Jiang, Y.-F., & Goodman, J. 2011, *ApJ*, **730**, 45
- Kara, E. 2018, *Natur*, **563**, 636
- Karakas, A. I. 2010, *MNRAS*, **403**, 1413
- Kauffmann, G., & Heckman, T. M. 2009, *MNRAS*, **397**, 135
- Kawakatu, N., Wada, K., & Ichikawa, K. 2020, *ApJ*, **889**, 84
- Kim, C.-G., & Ostriker, E. C. 2015, *ApJ*, **802**, 99
- Knapp, G. R. 1975, *AJ*, **80**, 111
- Knapp, G. R., Faber, S. M., & Gallagher, J. S. 1978, *AJ*, **83**, 11
- Kokusho, T., Kaneda, H., Bureau, M., et al. 2017, *A&A*, **605**, A74
- Kokusho, T., Kaneda, H., Bureau, M., et al. 2019, *A&A*, **622**, A87
- Koprowski, M. P., Dunlop, J. S., Michałowski, M. J., et al. 2017, *MNRAS*, **471**, 4155
- Kuntschner, H., Emsellem, E., Bacon, R., et al. 2010, *MNRAS*, **408**, 97
- Lang, P., Schinnerer, E., Smail, I., et al. 2019, *ApJ*, **879**, 54
- Levin, Y., & Beloborodov, A. M. 2003, *ApJL*, **590**, L33
- Lu, J. R., Do, T., Ghez, A. M., et al. 2013, *ApJ*, **764**, 155
- Mathis, J. S., Rimpl, W., & Nordsieck, K. H. 1977, *ApJ*, **217**, 425
- McKinnon, R., Torrey, P., & Vogelsberger, M. 2016, *MNRAS*, **457**, 3775
- Morozova, V., Piro, A. L., & Valenti, S. 2018, *ApJ*, **858**, 15
- Nagai, T., Marconi, A., & Maiolino, R. 2006, *A&A*, **447**, 157
- Negri, A., Pellegrini, S., & Ciotti, L. 2015, *MNRAS*, **451**, 1212
- Nomoto, K., Kobayashi, C., & Tominaga, N. 2013, *ARA&A*, **51**, 457
- Novak, G. S., Ostriker, J. P., & Ciotti, L. 2011, *ApJ*, **737**, 26
- Ostriker, J., & Silk, J. 1973, *ApJ*, **184**, L113
- Ostriker, J. P., Choi, E., Ciotti, L., Novak, G. S., & Proga, D. 2010, *ApJ*, **722**, 642
- Palla, M., Calura, F., Fan, X., et al. 2020, *MNRAS*, **494**, 2355
- Pellegrini, S. 2012, in *Hot Interstellar Matter in Elliptical Galaxies*, Astrophysics and Space Science Library, Vol. 378, ed. D.-W. Kim & S. Pellegrini (New York: Springer), **21**
- Pipino, A., Fan, X. L., Matteucci, F., et al. 2011, *A&A*, **525**, A61
- Reynolds, C. S., Balbus, S. A., & Schekochihin, A. A. 2015, *ApJ*, **815**, 41
- Saitoh, T. R. 2017, *AJ*, **153**, 85
- Sarzi, M., Alatalo, K., Blitz, L., et al. 2013, *MNRAS*, **432**, 1845
- Sarzi, M., Falcón-Barroso, J., Davies, R. L., et al. 2006, *MNRAS*, **366**, 1151
- Sazonov, S. Y., Ostriker, J. P., Ciotti, L., & Sunyaev, R. A. 2005, *MNRAS*, **358**, 168
- Schreiber, C., Elbaz, D., Pannella, M., et al. 2018, *A&A*, **609**, A30
- Schurer, A., Calura, F., Silva, L., et al. 2009, *MNRAS*, **394**, 2001
- Seab, C. G., & Shull, J. M. 1983, *ApJ*, **275**, 652
- Seitzzahl, I. R., Ciaraldi-Schoolmann, F., Röpke, F. K., et al. 2013, *MNRAS*, **429**, 1156
- Shakura, N. I., & Sunyaev, R. A. 1973, *A&A*, **24**, 337
- Sijacki, D., Vogelsberger, M., Genel, S., et al. 2015, *MNRAS*, **452**, 575
- Smercina, A., Smith, J. D. T., Dale, D. A., et al. 2018, *ApJ*, **855**, 51
- Smith, R. K., Krzewina, L. G., Cox, D. P., Edgar, R. J., & Miller, W. W., III 1996, *ApJ*, **473**, 864
- Steidel, C. C., Adelberger, K. L., Shapley, A. E., et al. 2003, *ApJ*, **592**, 728
- Stone, J. M., Gardiner, T. A., Teuben, P., Hawley, J. F., & Simon, J. B. 2008, *ApJS*, **178**, 137
- Tadaki, K., Iono, D., Yun, M. S., et al. 2018, *Natur*, **560**, 613
- Toomre, A. 1964, *ApJ*, **139**, 1217
- van Dokkum, P. G., & Franx, M. 1995, *AJ*, **110**, 2027
- Wang, T., Schreiber, C., Elbaz, D., et al. 2019, *Natur*, **572**, 211
- Weingartner, J. C., & Draine, B. T. 2001, *ApJ*, **548**, 296
- Xu, F., Bian, F., Shen, Y., et al. 2018, *MNRAS*, **480**, 345
- Yang, H.-Y. K., & Reynolds, C. S. 2016, *ApJ*, **818**, 181
- Yuan, F., Yoon, D., Li, Y., et al. 2018, *ApJ*, **857**, 121
- Zhukovska, S., Dobbs, C., Jenkins, E. B., & Klessen, R. S. 2016, *ApJ*, **831**, 147